Flinders
UNIVERSITY

Investigating the electronic structure of pentlandite by simulation of XPS 2p and NEXAFS $L_{2,3}$ spectra

---

Supervisor: Dr. Sarah Harmer

A Thesis Submission for Bachelor of Science (Honours)

By Simon Lee

Acknowledgments

I thank the Flinders University School of Chemical & Physical Sciences for giving me the opportunity to undertake an Honours project.

I thank the cohort of 2016 CaPS Honours students for their camaraderie and support, especially throughout coursework.

I thank my family for their ever-continual support of my academic endeavours.

I thank Frank de Groot for his correspondence in helping me understand the finer details of the software I used in this study.

I thank my research group colleagues Connor Retallick, Zoe Pettifer, Belinda Bleeze, and Sian La Vars for their help throughout the year. Your insight, feedback, and academic knowledge has been indispensable, and I've thoroughly enjoyed becoming part of this family.

Finally and most significantly I thank Sarah Harmer for being my supervisor on this project. Your guidance has been thoroughly valued and your confidence and reassurance has been indelibly beneficial. Thank you for making this year possible.

Declaration

Other than where duly referenced in the text, the material presented in this thesis is the original work of the author.

Simon Lee

Simon Lee

9/11/16

Abstract

Pentlandite is an iron-nickel sulfide mineral, important due being the world's most abundant source of nickel. For effective and efficient mineral processing of pentlandite through froth flotation a good understanding of its electronic structure is desirable. This study investigated the electronic structure of synthetic pentlandite through computational simulation of high-resolution XPS $2p$ and NEXAFS $\mathrm{L}_{2,3}$ spectra. A set of electronic structure parameters was determined which reproduced the spectral lineshapes observed in data. A charge-transfer pre-edge peak was observed in Fe NEXAFS and succesfully simulated showing a ligand $3p$ to iron $3d$ transition. The charge-transfer energy Δ of the system was shown to have an upper bound of 1 eV. Secondary peaks in Ni NEXAFS were shown to be due to multiplet splitting. Consistenly observed features in Ni XPS were shown to be charge-transfer satellites strongly dependant on the core hole potential.

Contents

List of Figures

1 Introduction

1.1 Pentlandite

Pentlandite is an iron-nickel sulfide mineral with the chemical formula $(\text{Fe}, \text{Ni})_9\text{S}_8$[1]. It's the most common source of nickel in the mining industry[1], and in 2015 Australia was the 4th largest producer of nickel worldwide[2]. Froth flotation is the most commonly used process to separate pentlandite from other minerals it's often found intergrown with, most commonly pyrrhotite ($\text{Fe}_{0.8-1}\text{S}$). This process separates minerals by the grinding bulk ore, mixing it in to water, and introducing hydrophobic substances that selectively attach to the minerals. The mixture is aerated, the hydrophobic particles attach to bubbles, and are floated to the surface. To determine which additives are needed to perform this procedure to the highest efficiency and effectiveness it is desirable to have a good understanding of the electronic properties of the mineral. Furthermore novel applications of the mineral have the chance to be identified when a good understanding of its electronic structure is achieved. The crystal structure of pentlandite is well-known[3], but its electronic structure is poorly understood[4].

In pentlandite, the metal atoms (iron and nickel) are bound to sulfur atoms either in an octahedral or tetrahedral coordination, as shown in Figure 1 (a). The crystal structure of pentlandite was proposed in 1936 by Lindqvist *et. al.* from analysis in powder form[5], later confirmed by Pearson 1956[3]. In a unit cell (the sub-structure repeated throughout the crystal) there are 4 octahedrally coordinated metals and 32 tetrahedrally coordinated[6], configured as shown in Figure 1 (b). Thus the tetrahedral and octahedral sites exist in an 8:1 ratio. Some studies have found evidence that there may be a preference for iron in the octahedral sites of natural pentlandite[7;8]. Otherwise for synthetic pentlandites such as used in this study there is no evidence to indicate an ordering of iron and nickel atoms in the metal sites, so they are modelled as being randomly distributed.

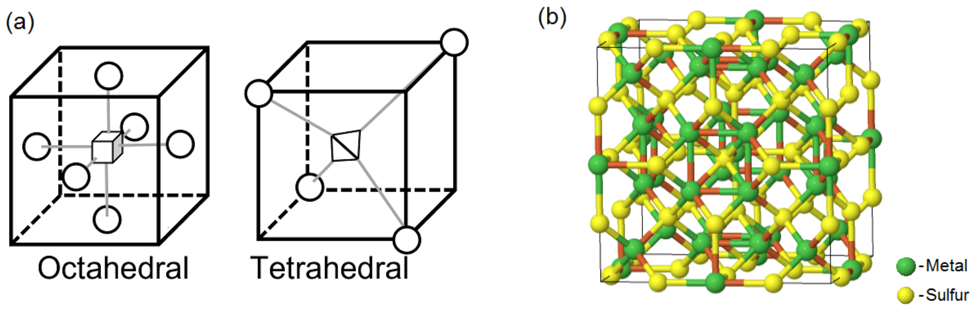

Figure 1: Geometry of octahedral and tetrahedral coordination (a) and pentlandite crystal structure (b)

To study the electronic structure of pentlandite, X-ray Photoelectron Spectroscopy (XPS) and Near Edge X-ray Absorption Fine Structure (NEXAFS) have previously been used. XPS is a technique wherein X-rays are directed at a surface in order interact with and eject electrons. Their kinetic energies are then analysed to identify which orbitals they occupied. In NEXAFS the energy of the incident X-rays is varied and their absorption is measured, allowing for detection of electrons transitioning in to unoccupied orbitals. These techniques complement each other to give a large amount of information on both the occupied and unoccupied orbitals in a system. In conjunction with these techniques spectral simulation software is used in an attempt to quantify the electronic parameters of the mineral's crystal structure, such as its crystal field splitting, charge transfer, and ligand covalent mixing energy.

1.2 Previous studies

With the increasing availability of lab-scale XPS instruments, in 1989 Richardson and Vaughan performed a study analysing (amongst others) the iron and nickel XPS spectra of synthetic pentlandite under multiple oxidation conditions[1]. They identified a single Fe $2p_{3/2}$ peak under standard unoxidised conditions, but otherwise didn't perform any further electronic structure analysis of unoxidised pentlandite. One of the conclusions of the study was that iron on the surface of synthetic pentlandite strongly preferentially oxidises relative to nickel.

Further XPS study was undertaken by Buckley and Woods in 1991[9]. A "clean" surface must be obtained to accurately analyse a bulk mineral through surface analytical techniques, i.e. it must have no contaminants, especially oxygen. At the time previous studies[10] had indicated that vacuum-fracturing natural sulfide mineral samples through impact lead to spectra that showed high levels of oxidation. From this it was inferred that these fractures naturally occurred along pre-oxidised interfaces. Initially a natural pentlandite sample was abraded in a nitrogen-flushed glove box. The Fe $2p$ spectrum showed a significant oxidation peak. The nickel spectrum however showed no noticeable oxidation, indicating that the iron-oxidation preference holds for natural pentlandite.

The first attempt at a more in-depth spectral characterisation of pentlandite was by Legrand *et. al.* in 1997[11]. A natural specimen of pentlandite encased in millerite was fractured in a vacuum and its oxidation was compared to that from other preparation methods. These included abrasion, polishing, chemical treatment, and regular vacuum fracturing. A significant O $1s$ peak was seen in the survey spectrum but was attributed mostly to water, thus the surface was considered to be virtually free of oxygen.

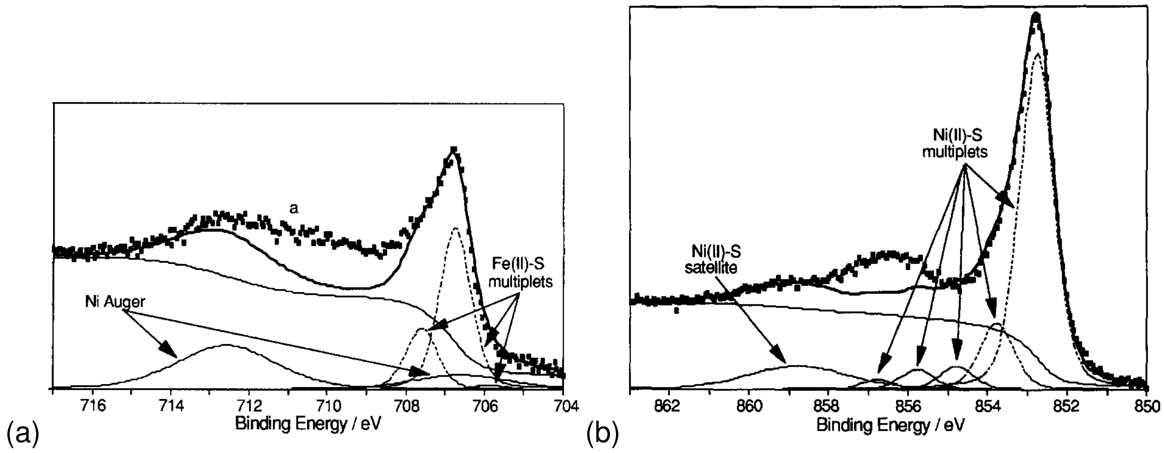

Figure 2: Fe XPS characterisation (a), and Ni XPS characterisation (b) by Legrand *et. al.* 1997[11].

Higher-energy broadening in both the iron (Figure 2 (a)) and nickel (Figure 2 (b)) spectra was attributed to either multiplet splitting (as calculated by Gupta and Sen[12]) or from a metallic asymmetric lineshape, but not all spectral features could be accounted for. Furthermore features present in the sulfur XPS spectrum were attributed to the binding energy difference between 4-coordinate and 5-coordinate sulfurs in the crystal structure.

With the increasing accessibility of synchrotrons for extremely high brilliance X-rays Goh *et. al.* performed a study in 2006[13] of abraded pentlandite, obtaining high-resolution Fe, Ni, and S K-edge NEXAFS spectra. Of particular note was the conclusion that the features attributed to sulfur coordination in Legrand's study were in fact due to an oxidation effect, presumed to be the formation of violarite ($\mathrm{Fe}^{2+}\mathrm{Ni}_2^{3+}\mathrm{S}_4$) on the surface. Furthermore, the measured pentlandite sulfur K-edge NEXAFS spectrum was simulated using both FEFF8 and WIEN2k codes. These codes use Mean field Theory and Density Functional Theory respectively to calculate spectra and electronic structure of solids. An upper bound of the binding energy difference between 4 and 5 coordinate sulfur in pentlandite was determined.

In 2010[14], Acres *et. al.* performed various synchrotron-based analytical techniques to image abraded pentlandite amongst chalcopyrite (CuFeS_2) and pyrrhotite. From these, Fe L-edge and Ni L-edge NEXAFS spectra were produced. Then iron NEXAFS spectrum showed a distinguishable pre-edge feature, attributed to "transitions of the Fe L_3 electrons to multiple unoccupied electron eigenstates just below the ionization threshold"[14].

The software used in this study, CTM4XAS, has previously been used to simulate the spectra of oxides and strongly correlated sulfides other than pentlandite[15–18]. Spectral features arising from multiplet splitting and charge transfer were reproduced and have shown good agreement with experimental results.

1.3 Project aim

The aim of this project is to investigate the electronic structure of pentlandite through analysis of metal XPS and NEXAFS spectra of a synthetic sample. Computational simulation of these spectra is used to quantitatively determine the value of certain electronic structure parameters. Furthermore the origin of certain spectral features is investigated through variation of these parameters.

2 Theoretical background

2.1 Surface analytical techniques

2.1.1 X-ray Photoelectron Spectroscopy

When a photon interacts with an electron the photon is absorbed and its energy is imparted to the electron. If the electron is bound to a nucleus in an atom this may cause it to jump to a higher energy orbital. However if the energy is large enough the electron will be ejected from the atom completely (described in Figure 3). This is known as the *photoelectric effect*, the process is known as *photoemission*, and the ejected electron is called a *photoelectron*.

X-ray Photoelectron Spectroscopy (XPS) is a surface-analytical technique which makes use of the photoelectric effect to measure the binding energy of electrons in a material. Monochromatic X-rays are fired at a surface with the intention of ejecting electrons. These electrons are captured and their kinetic energies are measured. Because the X-ray photon energy is known the binding energy $B.E.$ of the electron can be determined using Equation 1:

$$B.E. = h\nu - K.E. - \phi \tag{1}$$

where the energy of the incident photon is $h\nu$, the measured kinetic energy of the electron is $K.E.$, and the "work function" is ϕ (the amount of energy lost both through detector absorption and electron ejection from the surface). A spectrum of counts versus binding energies can then be plotted. This information can be used to identify which orbitals were occupied in the material, along with other more subtle effects.

XPS is typically performed in ultra-high vacuum due to the significant interactions between free electrons and air relative to the high experimental sensitivity. A vacuum chamber is thus put at the end of a radiation source in which samples can be placed. Emitted electrons are captured and (typically) passed through concentric hemispherical domes with voltages applied to them, described in Figure 3 (b). These voltages can be tuned to select for electrons of a certain velocity (and thus energy) before being detected.

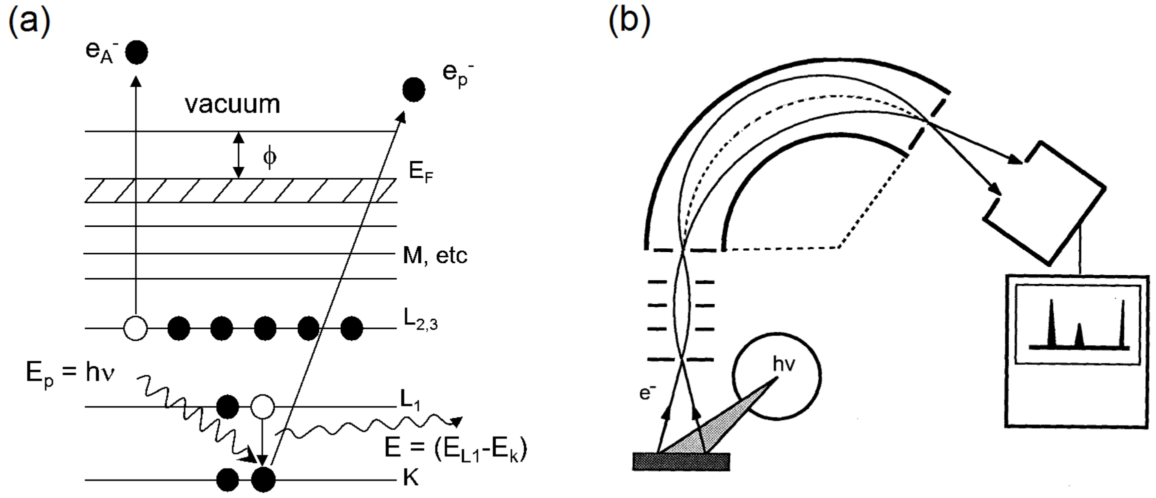

Figure 3: Photoemission process diagram (Harmer, personal communication) (a) Simplified XPS instrument setup, adapted from[19] (b)

The binding energy is, ostensibly, the “strength” with which the electron is “bound” to the atom. The closer to the nucleus the orbital is the higher the binding energy. What is technically meant by the “strength” of binding however is the amount of energy required to go from the initial state to a final state where the desired electron has been ejected. In short it’s the energy difference between the (short-term[1]*) initial and final states of the atom. This process doesn’t happen in isolation; various other intra-atomic and inter-atomic phenomena can affect the energy of the final state. Furthermore due to the nature of electrons as probability density functions (i.e. their behaviour is governed fundamentally by statistical probability) and the addition of energy to a system through temperature these changes to both initial and final state energies aren’t entirely consistent between any given atoms in a system. Measured XPS spectra are therefore convolutions of multiple initial and final state contributions with different magnitudes of probability.

XPS spectra can be convoluted and broadened from a number of different phenomena, both intrinsic and extrinsic to the surface[20]. Broadening due to the instrument can be due to the level of non-monochromaticity in the X-ray source, resulting in a range of kinetic energies for any one given binding energy. Further broadening occurs due to the non-infinitesimal selection range of the hemispherical analyser. These broadenings are known to follow Gaussian distributions[21]. Broadening intrinsic to the material is affected by the lifetime of the electron core hole (before

---

[1] *After some time (of the order of femtoseconds) an atom’s electronic structure will relax and many extra phenomena occur which change the eventual energy of the system but do not relate to the kinetic energy of the photo-emitted electron. These are not necessary to take in to account for simulation purposes.

the system relaxes and fills it) and the lifetime of the excited state. These vary dependant on the element and the absorption edge being measured and can be modelled with a Lorentzian distribution[22].

Convolution of the spectra (i.e. close spectral features overlapping significantly) has many origins. Assuming a pristine sample is analysed (so there are no oxidation features) convolution can occur due to artefacts from secondary emission events. Furthermore the element being analysed may exist in different bonding structures or ionisation states throughout the material. If a lower-energy X-ray is used penetration in to the surface may be shallow enough such that surface features are distinguishable from the bulk material. These all need to be taken in to account when interpreting XPS spectra.

For conventional XPS the X-rays may be produced by bombarding a metal with high-energy electrons and directing the emitted light through a monochromator. For example aluminium can be used to produce 1.487 keV K-alpha X-rays or magnesium for 1.254 keV rays. One of the downsides of this method is the intrinsic non-monochromaticity of these light sources, which results in a broader energy range of incident photons, but can be somewhat improved with the use of a monochromator. The resultant spectral broadening in typical conditions gives a full-width-half-maximum within the range of 0.3-1.7eV.

2.1.2 Near Edge X-ray Absorption Fine Structure

Near Edge X-ray Absorption Fine Structure (NEXAFS) is a technique where the incident photon energy is varied and the absorbance is measured[23]. NEXAFS is used to look at spectral fine structure close to the main absorption edge, as opposed to a technique such as EXAFS (extended X-ray absorption fine structure). Typically the measurements are made through a drain current, measuring the change in voltage versus the energy of the incident photons. When electrons are excited up to higher state (or ejected form the surface) a relaxation effect occurs shortly afterwards where the empty orbital is filled by some other higher energy orbital. The energy lost in this process can be emitted as a photon (fluorescence) or transferred to another electron. If this energy is high enough that electron is ejected; this is known as an “Auger electron”. Total Electron Yield, Partial Electron Yield (filtering out lower kinetic energy electrons), Auger Electron Yield, and Fluorescence Yield detection methods can all be used to create NEXAFS spectra.

As previously mentioned photoemission is merely one of many electron processes that occurs directly or indirectly due to interaction with a photon. At certain energies bound core electrons can be excited to higher unoccupied orbitals, whether they be unoccupied atomic or molecular orbitals, or at a high enough energy they can also be subject to photoemission. Typically when the incident photon energy is exactly equal to the binding energy of a core electron it will be excited to the lowest unoccupied orbital in the system. This gives a different final state compared to XPS where detection requires photoemission. Because of this difference in the states of the systems between XPS and XAS a set of parameters which can describe both is more reliable than simply satisfying the effects in one system.

To achieve the varying-energy X-ray source necessary for NEXAFS a synchrotron light source must be used. The basic theory behind synchrotron light is as follows. Electrons moving at constant velocity create a steady electromagnetic field. Accelerating electrons changing direction however create a toroidal-shaped changing field, or a wave (i.e. light). If travelling at relativistic speeds the geometry of this wave is distorted in to a highly collimated beam in the direction of motion. This is known as synchrotron light. Electrons are first accelerated to over 0.999999 c and synchrotron light is produced through the application of bending magnets, wigglers, undulators, or free electron lasers. This extremely bright and highly monochromatisable light is directed down “beamlines”, at the end of which detectors and other instruments can be placed. This technique allows for exceptionally high resolution spectroscopy. Depending on the sample and the orbitals being probed the broadening due to a synchrotron XPS setup can be at or below 0.25 eV[20].

2.2 Charge Transfer Multiplet theory

To accurately simulate the electronic structure of pentlandite a method that covers the various phenomena in a transition metal sulfide crystal system is required. Methods such as Hartree Fock, Density Functional Theory, and Mean Field Theory are known to be deficient at simulating the effects of strong correlation and charge transfer[24–26], which are behaviours expected in the transition metal sulfide nature of pentlandite. Furthermore, codes that implement these methods such as FEFF8 and WIEN2k calculate the states of single electrons independently and only consider the ground state of the atom, not the excited state. These deficiencies are successfully covered by the Charge Transfer Multiplet (CTM) method.

Strongly correlated systems are those where the motion of electrons strongly depends on the motion of other electrons in the same system, i.e. their positions are “correlated”. This can result in a higher energy system than expected from basic Hartree Fock calculations which assume an independence in electron position except for that due to the exchange interaction.

Charge transfer is the fluctuation of charge between bound atoms, which can change the short-term configuration during a photoemission process. Furthermore one of the distinguishing aspects of CTM is that it takes in to account the difference between initial and final states of a system during an experimental process.

The basic build-up of a bound atomic model in CTM is as follows. The free atomic state wavefunctions are initially calculated using Slater intergrals, and spin-orbit coupling is taken in to account. Crystal field parameters are introduced and assumed to stay consistent with that of the ground state of the atom. Charge transfer probabilities are then calculated with dependence on ligand covalent mixing, the Coulomb interaction strength between outer metal electrons, and the electric potential due to the core hole. A basic description of the theory behind these aspects is given, based on *Core level spectroscopy of solids* by de Groot and Kotani (2008)[27].

2.2.1 Atomic orbitals

The nature of electrons bound in an atom can fundamentally be understood as follows. Physical systems fundamentally tend towards the lowest possible energy. Electrons exist in discrete quantities as wavefunctions which have a distribution through space. When in the proximity of a nucleus (or a positive charge in general) an electron's lowest potential energy state is as a standing wave surrounding the nucleus, known as an *orbital*. The geometry of these waves is described using 3D spherical harmonic wavefunctions. In a single-atom system these orbitals can be perfectly described using four discrete variables known as *quantum numbers*.

The *principal quantum number* (n) describes which classical "shell" (as understood in the Bohr model) the electron occupies, effectively how "far away" it is from the nucleus, in a relative sense. The *azimuthal quantum number* (l), or *angular/orbital quantum number*, describes which classical "subshell" the electron occupies; typically a larger l indicates a more complex geometric structure with more symmetry elements. In a single-atom system all orbitals with the same n and l have the same energy and the same orbital angular momentum, and increasing either number represents a higher energy orbital. Because of this, groups of orbitals are described by listing their n and l, where l is represented by a letter ($l = 0 \to s,\ 1 \to p,\ 2 \to d,\ 3 \to f,\ 4 \to g...$), such as "$2s$" or "$3d$". For orbitals with quantum number n, l varies from 1 to n. For example, there are $3s$, $3p$, and $3d$ orbitals, but there is no $1p$, only $1s$.

The *magnetic quantum number* (m_l), which could be considered its *orbital angular momentum projection*, typically determines the orientation of the orbital relative to a predefined axis; all orbitals (aside from $m_l = 0$) with the same n and l have the same geometry, and varying m_l rotates them (as shown in Figure 4a). For orbitals with quantum number l, m_l varies from $-l$ to l (i.e. there are $2l+1$ options for m_l). The *spin projection quantum number* (m_s) describes the spin of an electron, an intrinsic angular momentum (i.e. not from rotation). m_s varies from $-s$ to s, where s is the spin quantum number, describing the magnitude of a particle's spin. For electrons, $s = \frac{1}{2}$. This means that for electrons there are two available m_s values; $\frac{1}{2}$ and $-\frac{1}{2}$, known as "spin *up*" and "spin *down*" respectively.

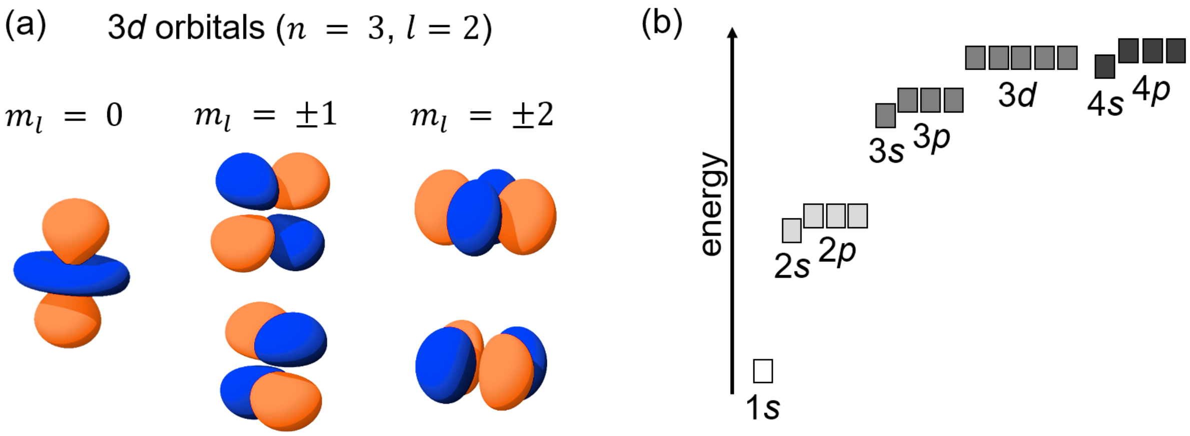

Figure 4: 3d orbital geometry showing high probability regions, adapted from Hatfield 2008[28](a) Orbital energy diagram (b)

The Pauli exclusion principle implies that no two electrons bound in the same atom may have identical quantum numbers. Thus when electrons are added to an atom they "fill up" an atom's unoccupied orbitals in order of their energy levels. In a single-atom system all available m values are filled first, followed by "pairing" where second electrons occupy the same orbital but with a complimentary spin (i.e. different s), a process described by Hund's rules. Pairing is less preferential due to electron-electron repulsion. As a rule whole shells are filled before filling further shells, and whole subshells are filled before filling further subshells. This isn't always the case, even in single-atom systems. For example the $4s$ orbitals are lower energy than the $3d$ orbitals (shown in Figure 4 (b)).

Iron has an atomic number of 26 (indicating the number of protons in the nucleus), and nickel's is 28. In both these elements every shell from the $1s$ to the $4s$ orbitals is completely filled (with 20 electrons). The remaining electrons partially fill the $3d$ orbitals, hence being $3d$ transition metals. In pentlandite the $4s$ electrons in both iron and nickel are using in the binding process with sulfur, making them Fe^{2+} and Ni^{2+} ions respectively. The $2p$ and $3d$ orbitals overlap significantly, which means that changes in the $3d$ structure also change the behaviour of electrons in the $2p$ orbitals due to electron-electron interactions.

2.2.2 Multiplet splitting

For an electron in a given set of orbitals (i.e. for a given n and l) its existence is parameterised by its orbital projection m_l and its spin projection m_s. For a single electron in an s orbital this gives two possible microstates; $m_l = 0$, and $m_s = -\frac{1}{2}$ or $\frac{1}{2}$. The number of microstates drastically increases with the number of electrons and options for angular momentum projection. For example, two electrons in the same set of p orbitals each have three options for m_l and 2 for m_s. Electrons are known to be "identical particles", or "indistinguishable particles", meaning that even in principle there is literally no difference between two electrons occupying two states and having their states swapped. Therefore, combinations and not permutations are used to calculate the number of possible microstates. There are six different ways for two indistinguishable particles to occupy three spaces ($3 \cdot 2 \cdot 1$), and four different ways for the spins to exist (both spin up; both spin down; former up latter down; former down latter up), giving 24 potential microstates. Of these, three are identical states (one up and one down in the same space), and due to the Pauli exclusion principle the three up-up pairs and down-down pairs can be excluded. This leaves 15 viable microstates for a two p-electron system, shown in Figure 5.

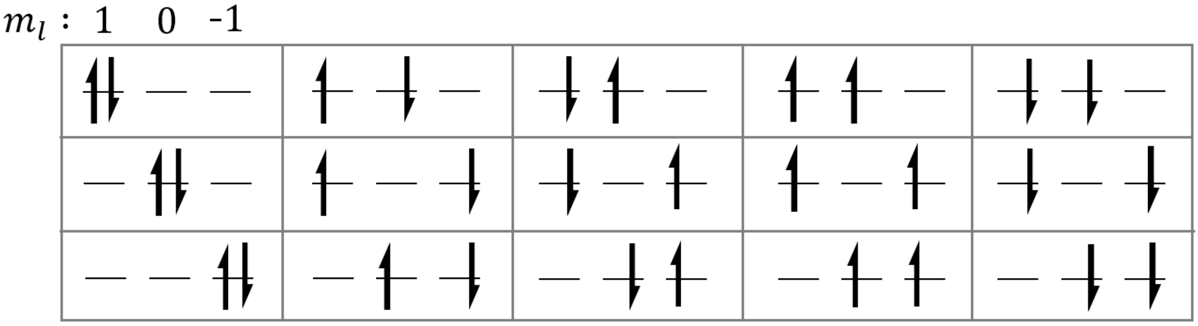

Figure 5: All configuration possibilities for 2 p-orbital electrons

The ground state (the state with the lowest energy) is, according to Hund's rules, the one with the lowest electron-pairing (dependant on the magnitude of the addition of all spin projections), then highest orbital angular momentum (the magnitude of the addition of m_l values), then lowest spin-orbit coupling (dependant on the addition of the previous two). While the ground state has the highest probability of being detected, in a probabilistic system with heat (such as electrons in an atom at room-temperature) the non-ground state configurations at higher energy levels potentially have a non-zero probability. Indeed, experimentally many systems have shown additional spectral structure due to these so-called "multiplet" states.

This effect is amplified due to the inducing of further states in the final state configuration of an XPS or XAS experiment. For instance, the initial state Fe^{2+}is $1s^2 2s^6 2p^6 3s^2 3p^6 3d^6$. The filled orbitals only have 1 possible state, so they have no effect on the multiplet structure. Thus, Fe^{2+} can be said to be in a $3d^6$ configuration. This already has $\frac{10!}{(10-6)!6!} = 210$ microstates. In an XPS experiment where a a $2p$ electron is ejected to form a $2p^5 3d^6$ configuration, this gives 1260 final state configuration. While some of these states may have zero probabilities depending on the system, and some energies may be degenerate, and some transitions from initial to final state configurations may no be allowable through selection rules, this results in a very large number of different energy differences between initial and final states. The phenomenon of these many energies appearing in spectra is called “multiplet splitting”.

In essence, multiplet splitting is due to the spin-spin coupling and orbital projection interactions of electron systems in unfilled orbitals. Physically this is arises due to the localisation of $3d$ orbitals and the strong overlap of $2p$ and $3d$ orbitals in $3d$ transition metals.

2.2.3 Spin-orbit coupling

Electrons have angular momentum both from intrinsic spin and from its orbit around the nucleus. While not a realistic description of the system, this is analogous to a planet which is orbiting around a sun while also rotating on its own axis (Figure 6). For $2p$ electrons if the orbital and spin angular momenta are aligned it exists in a $2p_{\frac{3}{2}}$, as $l + s = 1 + \frac{1}{2} = \frac{3}{2}$. If they are antiparallel, it’s in a $2p_{\frac{1}{2}}$ state. Because a charged particle with angular momentum creates an electromagnetic field which interacts with the local , differing magnitudes of the total angular momentum result in different binding energies. As there are two options the singlet state of a group of orbitals splits in to a doublet. The peak area ratio is determined by the $2(l + s) + 1$ degeneracy, meaning that the $2p_{\frac{3}{2}}$ peak with be twice as large as the $2p_{\frac{1}{2}}$ peak.

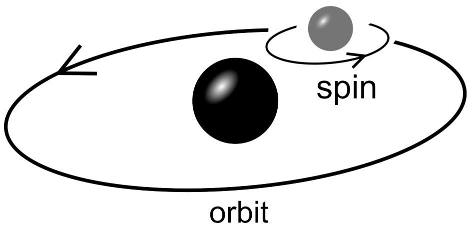

Figure 6: Planetary system analogous to electron orbital and intrinsic angular momentum

2.2.4 Crystal field splitting

The $3d$ orbitals have a directionality to them such that the internal electronic structure of the atom is influenced by the local symmetry conditions. Some of the metals sites in pentlandite are bound octahedrally to 6 ligands, in this case to sulfurs. Three of the $3d$ orbitals are oriented orthogonally to each other such that they can be positioned between the ligands. These three are known as the t_{2g} orbitals (shown in Figure 7b). The remaining two orbitals are thus oriented such they they are directly positioned towards the ligands. These are known as the e_g orbitals (shown in Figure 7a). Due to the lower electron-electron interactions the t_{2g} orbitals have a lower energy level (shown in Figure 7c), and therefore are preferentially filled compared to the e_g orbitals.

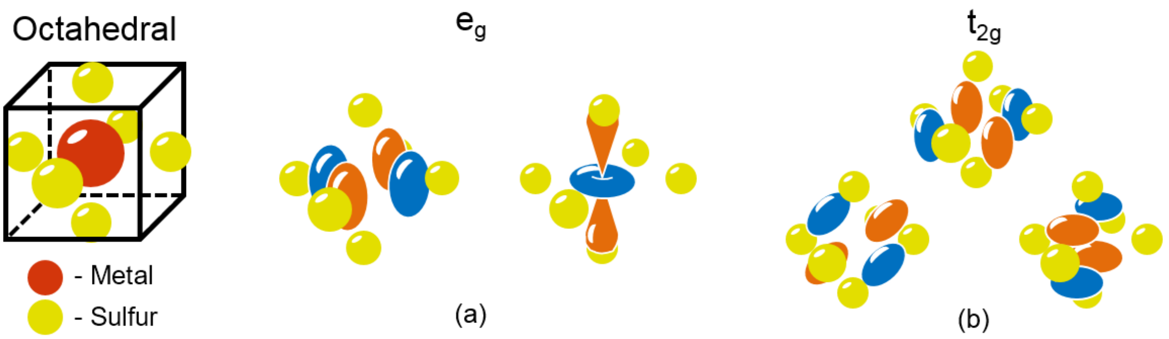

Figure 7: Octahedral coordination and the relative positions of e_g (a) and t_{2g} (b) orbitals

Metals can also be tetrahedrally coordinated to sulfur ligands. In this case, the t_{2g} orbitals (Figure 8a) interact more strongly with the ligands than the e_g orbitals (Figure 8b) do. As such their energy levels are reversed (Figure 8c) relative to those in octahedral coordination.

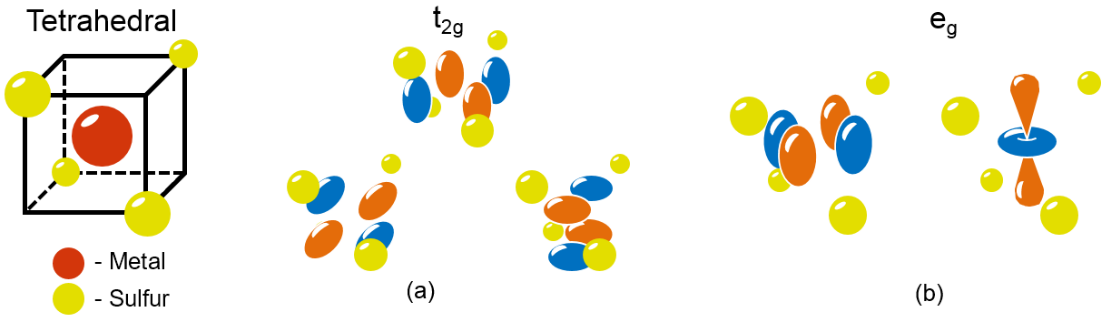

Figure 8: Tetrahedral coordination and the relative positions of t_{2g} (a) and e_g (b) orbitals

The energy difference between the t_{2g} and e_g orbitals is known as the ligand field splitting or crystal field splitting, and in octahedral coordination is labelled as Δo or $10Dq$ (Figure 9a). The magnitude of the crystal field splitting in tetrahedral coordination (Δt) is less than in octahedral (Figure 9b) due to a less distinct directionality towards to the ligands. Additionally, because the

t_{2g} orbitals are at a higher energy than the e_g in tetrahedral coordination, the value of the crystal field splitting is negative. The symmetry of the system is otherwise the same, both belonging to the O$_h$ point group. Theoretically, for free systems, $\Delta t = -\frac{4}{9}\Delta o$.

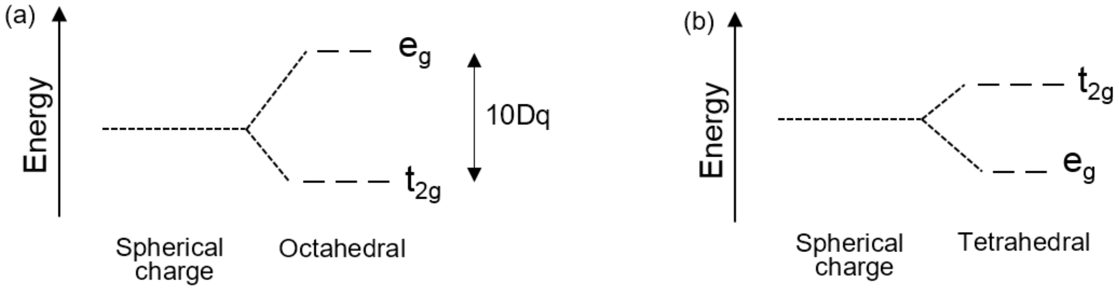

Figure 9: Splitting of t_{2g} and e_g energy levels relative to a spherical charge distribution for octahedral (a) and tetrahedral (b) coordination

It's evident that crystal field splitting further splits the energy levels of the outer level electrons, a more significant effects also becomes apparent. The "pairing energy" of a system is simply the energy required to pair two electrons. More specifically it's the difference in energy between a state where an additional electron is paired with another electron (such as when all m states have been filled) or the additional electron fills the next completely unoccupied orbital. Typically it's preferential for an electron not to pair up due to the strength of electron-electron interactions, unless of course the next available m state also requires a change in n and/or l. If however the crystal field splitting energy is larger than the pairing energy, pairing will be the preferred option. Two different possibilities then emerge: the "high spin" state where its preferable not to pair up (thus increasing the number of unpaired spins), or the "low spin" state wherein pairing is preferential to occupying the higher energy orbital (Figure 10).

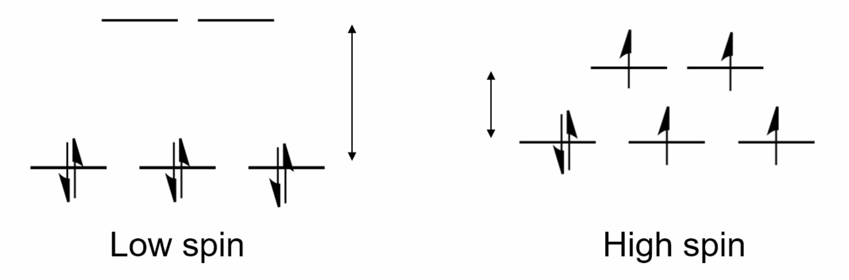

Figure 10: Diagram of $3d$ occupation in low spin and high spin $3d^6$ systems

2.2.5 Charge transfer

Charge transfer effects are fluctuations of charge in a material both in its initial and final states. Charge (specifically electrons) can shift between the metal and the ligand, in this case typically from the sulfur $3p$ to the metal $3d$ orbitals. This doesn't necessarily occur throughout and entire solid structure due to the inherent probabilistic nature of electron position and interaction, so the occur occurrence of charge transfer in its multiple states results in a statistical distribution of initial and final states with charge transfer of varying degrees. The most significant occurrence of charge transfer is after a photoemission event. It's may be a favourable transition for a sulfur $3p$ electron to transfer in to the partially filled metal $3d$ band to "screen" the effect of the core hole by reducing the unpaired spin nature of the material. Depending on the probability distributions the electron may transfer in to either the t_{2g} or e_g orbitals. As with other effects the increased number of potential initial and final states of the system can significantly change the complexity of spectra. The effects of charge transfer are strongly affected by the strength of the electric potential due to the core hole, the strength of Coulomb interactions between valence electrons, and the mixing of outer orbitals between the metal and the ligand.

3 Methods

3.1 Data

3.1.1 XPS and NEXAFS data

A sample of synthetic pentlandite was made with a stoichiometry of $\mathrm{Fe}_{4.35}\mathrm{Ni}_{4.56}\mathrm{S}_{8.08}$. The structure was confirmed to be that of pentlandite through X-ray diffraction and the stoichiometry was determined through electron microprobe analysis. Synthetic pentlandite was used to ensure a controllable Fe:Ni ratio. The sample was taken to the Australian Synchrotron in 2014. To analyse a pristine pentlandite surface the sample was mounted and placed in a vacuum chamber. The chamber was kept at or below $2 \cdot 10^{-10}$ Torr, and the sample was notched and mechanically cleaved to produce a pristine surface. The main alternative used in prior studies, abrasion, has been shown to still display significant oxidation and adventitious carbon contamination. Additionally, in earlier studies vacuum fracturing was achieved through impact rather than using a machine.

Both XPS and NEXAFS measurements were taken at the Australian Synchrotron's soft X-ray beamline (SXR, 14ID). To obtain a monochromatic signal the X-rays were passed through Peterson plate grating monochromator (1200 lines per mm). The photon flux ranged from $5 \cdot 10^{11}$ to $3 \cdot 10^{12}$ photons per second per 200mA, with an approximate spot size of 0.6mm^2. A pentlandite XPS survey spectrum was obtained with an incident X-ray energy of 1486.7 and an energy step size of 0.5 eV. Fe $2p$ and Ni $2p$ XPS spectra were collected with a photon energy of 1475 eV and a step size of 0.025 eV. Fe $L_{2,3}$ and Ni Fe $L_{2,3}$ NEXAFS spectra were measured with a step size of 0.1eV and a dwell time of 1 second. The "$L_{2,3}$" spectrum refers to the L_2 and L_3 absorption edges in XAS spectra, equivalent to the $2p_{\frac{1}{2}}$ and $2p_{\frac{3}{2}}$ peaks in XPS.

3.1.2 Processing

XPS data was processed in Casa XPS. The Fe $2p_{\frac{3}{2}}$ peak was calibrated to 706.8 eV and the Ni $2p_{\frac{3}{2}}$ peak was calibrated to 853.2 eV as measured by Acres et al[14]. Regions were created encompassing all visible spectral features. Shirley backgrounds are known to be approximately accurate and realistic background subtractions for XPS in most circumstances[29]. A single Shirley background was taken for Fe XPS, but a single Shirley background was unrealistic for Ni as it exceeded the magnitude of the data at points. A second Shirley background was started at 864 eV for the Ni XPS data.

NEXAFS data was processed using Athena. The pre- and post-edge regions had a linear background removed to result in zero slope and a further arc-tangent background was removed[30]. The centre of the arctan slope was placed at the centre of the L_3 peak and its width was determined by the intrinsic broadening of the synchrotron source (estimated to be 0.15 eV). The magnitude of the subtracted background was determined such that the lowest post-edge region was reduced to zero.

3.2 Simulation

To investigate the electronic structure of pentlandite it is desired to identify the values of quantifiable electronic parameters that describe the crystal system. Software can be used to simulate XPS and NEXAFS spectra using quantifiable parameters as variables. If a single set of values for these parameters can accurately recreate the features data obtained in different experiments that induce distinct states and measure different information then these results can be considered scientifically valid.

CTM4XAS is software the can simulate XAS (X-ray absorption spectroscopy) and XPS spectra (amongst others) for a number of transition metals in various levels of ionisation and in different bonding geometries authored by Eli Stavitski and Frank de Groot[31], with the original source code written by Theo Thole and modified by Haruhiko Ogasawara. The code is based on the Charge Transfer Multiplet method for spectral simulation. Technically the software is an interface to a set of sub-programs which work in series, with each output subsequently fed to the next program. The base atomic energy level calculations are made by RCN2, dependant on the element, level of ionisation, and the initial and final states expected from the experimental method. These are augmented by introducing atomic multiplet effects and spin-orbit coupling with RCG2. Crystal field splitting effects are then calculated using RAC2. The final spectrum with charge-transfer multiplets is calculated through BAN2. The result of these programs is an output of "sticks"; a list of energies indicating the predicted binding energies in XPS or the predicted transitions in XAS, with relative magnitudes of their likely distributions. To make a simulated spectrum a combined Gauss-Lorentz distribution is applied at each of these energies, and all the peaks are added together to create the final simulated spectrum.

The broad method in which this software can be used to determined the electronic structure parameters of pentlandite is as follows. For a given electronic configuration and analytical technique the electronic structure parameters are systematically varied to determine the effect they have of the resultant spectrum, both individually and . Through an iterative processes of exploratory testing a set of parameters is settled upon that reasonably-well replicate the features seen in the given data. Theoretically these parameters need to give realistic simulation results regardless of the analytical method. A different technique is then simulated using the same parameters to determine their appropriateness. If the simulation does not agree with results a continuation of the iterative process is undertaken. Through many iterations of parameter optimisation for both analytical techniques eventually converges on a solution, within a certain small range of acceptability. Furthermore in a material such as pentlandite where the distribution of iron and nickel (both $3d$ transition metals) is assumed to be random throughout the available metal sites these parameters are expected to be appropriate for both minerals. With two electronic configurations, two analytical techniques for each, and one set of electronic structure parameters to describe all four systems, the final values can be considered to be scientifically robust. While a mathematical proof of the uniqueness of this solution isn't evident, it is considered extremely unlikely that a significantly different set of parameters within the real of reasonable solutions would provide a successful solution. A description of the simulation process and parameters is given, based on *Core level spectroscopy of solids* by de Groot and Kotani (2008)[27].

3.2.1 CTM4XAS

The fundamental equation in the interaction between X-rays and matter is the Golden Rule. The probability W of a transition between an initial state Φ_i and a final state Φ_f from a photon impact of energy $\hbar\Omega$ is shown in Equation 2:

$$W_{fi} = \frac{2\pi}{\hbar} \left| \langle \Phi_f | \, T \, | \Phi_i \rangle \right|^2 \delta(E_f - E_i - \hbar\Omega) \tag{2}$$

where E is the state's energy and T is the transition operator. $\frac{2\pi}{\hbar}$ is a scaling factor and the δ function ensures a conservation of momentum. The overall task of the software is to calculate the wavefunctions for the initial and final states of a system and solve for the transition probability over a range of energies for a given set of electronic structure parameters.

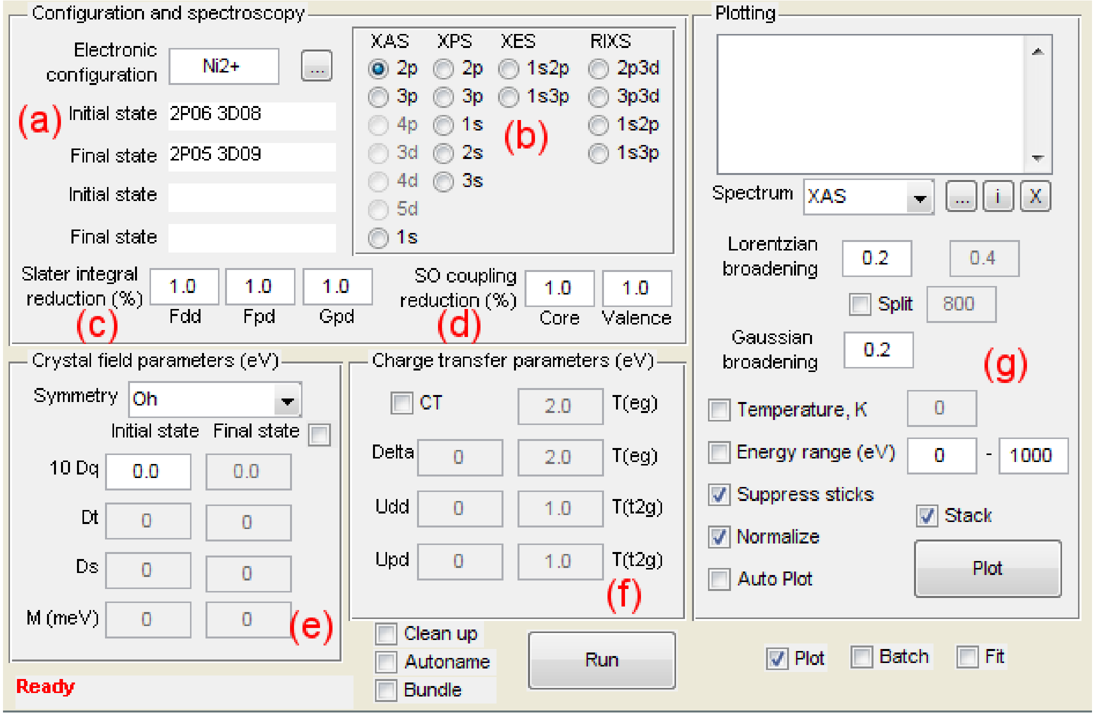

Configuration and spectroscopy
Electronic configuration: Ni2+
Initial state: 2P06 3D08
Final state: 2P05 3D09
Initial state:
Final state:
XAS: ● 2p ○ 3p ○ 4p ○ 3d ○ 4d ○ 5d ○ 1s
XPS: ○ 2p ○ 3p ○ 1s ○ 2s ○ 3s
XES: ○ 1s2p ○ 1s3p
RIXS: ○ 2p3d ○ 3p3d ○ 1s2p ○ 1s3p
Slater integral reduction (%): Fdd 1.0, Fpd 1.0, Gpd 1.0
SO coupling reduction (%): Core 1.0, Valence 1.0

Crystal field parameters (eV)
Symmetry: Oh
Initial state / Final state ☐
10 Dq: 0.0 / 0.0
Dt: 0 / 0
Ds: 0 / 0
M (meV): 0 / 0

Charge transfer parameters (eV)
☐ CT
2.0 T(eg)
Delta: 0, 2.0 T(eg)
Udd: 0, 1.0 T(t2g)
Upd: 0, 1.0 T(t2g)
☐ Clean up
☐ Autoname
☐ Bundle

Ready

Plotting
Spectrum: XAS
Lorentzian broadening: 0.2, 0.4
☐ Split: 800
Gaussian broadening: 0.2
☐ Temperature, K: 0
☐ Energy range (eV): 0 - 1000
☑ Suppress sticks
☑ Normalize
☐ Auto Plot
☑ Stack
☑ Plot ☐ Batch ☐ Fit

Figure 11: Interface of CTM4XAS with sections labelled

The interface of CTM4XAS is shown in Figure 11. (a) allows for control of the element and its level of ionisation, along with displaying the expected initial and final states dependant on the analytical technique and desired peaks to be simulated as selected in (b). These are the segments calculated by RCN2. (c) controls the reduction in Slater-Condon parameters relative to their values as calculated in the Hartree-Fock method, and (d) controls the reduction of spin-orbit coupling strength. These parameters are used by RCG2. The symmetry of the local crystal geometry, along with the strength of the relevant crystal field splitting, is controlled in (e). Changes in the crystal field in the final state, along with parameters relevant to more complex symmetry groups, are also available. These parameters are used by RAC2. The last set of parameters, relating to charge transfer (which can be toggled on or off), are controlled in (f) and used in BAN2. The Lorentzian broadening, Gaussian broadening, and temperature are controlled in (g) and are used to plot spectra once the sticks are calculated.

Slater integral reduction Fundamentally to calculate the energy of any quantum system one needs to solve the Schrödinger Equation (Equation 3).

$$H\Psi = E\Psi \tag{3}$$

where Ψ is the quantum wave function describing the system, H is the Hamiltonian (the energy operator for the system), and E is the energy of the system. The Hamiltonian for a single non relativistic particle is given in Equation 4:

$$H = \frac{-\hbar}{2\mu}\nabla^2 + V(r) \tag{4}$$

with the first and second terms being the kinetic and potential energies respectively. In the case of an electron bound to a nucleus this can be written as in Equation 5:

$$H_{bound\,electron} = \frac{p^2}{2m} + \frac{-Ze^2}{r} \tag{5}$$

where p is the electron's momentum, m is the mass of an electron, Z is the number of protons in the atom's nucleus, e is the charge of an electron, and r is the radius of its orbit. Summing over all the electrons in an atom, a rudimentary Hamiltonian for a free atom can be given as in Equation 6:

$$H_{free\,atom} = \sum_N \frac{p_i^2}{2m} + \sum_N \frac{-Ze^2}{r_i} \tag{6}$$

The electron-electron repulsion interaction $\frac{e^2}{r}$ is added in for the calculation of multiplet splitting, giving Equation 7.

$$H_{free\,atom} = \sum_N \frac{p_i^2}{2m} + \sum_N \frac{-Ze^2}{r_i} + \sum_{pairs} \frac{e^2}{r_{ij}} \tag{7}$$

The wavefunctions are calculated as Slater determinants, and the expansion of the electron-electron interaction term gives the Slater-Condon parameters F and G shown in Equation 8.

$$\left\langle {}^{2s+1}L_j \right| \frac{e^2}{r_{12}} \left| {}^{2s+1}L_j \right\rangle = \sum_k f_k F^k + \sum_k g_k G^k \tag{8}$$

The F term is for the Coulomb multipole interaction (the static electric repulsion between electrons) and the G term is for the exchange multipole interaction (fundamentally the difference in energy between two spin-parallel and spin-antiparallel electrons). In CTM4XAS, F_{dd}

(between d-orbital electrons), F_{pd}, and G_{pd} (between valence and core electrons) can be modified to reduce the magnitude of these parameters from those calculated in the Hartree-Fock method. By default they are reduced to 80% of their original values. In essence these parameters control the magnitude of the multiplet splitting.

Spin-orbit coupling The coupling of intrinsic angular momentum and orbital angular momentum is added $(l \cdot s)$ with an empirical scaling factor ζ, as shown in Equation 9:

$$H_{free\,atom} = \sum_N \frac{p_i^2}{2m} + \sum_N \frac{-Ze^2}{r_i} + \sum_{pairs} \frac{e^2}{r_{ij}} + \sum_N \zeta(r_i) l_i \cdot s_i \tag{9}$$

CTM4XAS allows for changing the spin-orbit coupling parameters for both the valence and core electrons, however typically the core electrons are well-shielded enough that their parameter is always set to default. The strength of the spin-orbit coupling primarily determined the width of the splitting between, for example, $2p_{\frac{3}{2}}$ and $2p_{\frac{1}{2}}$ peaks. With this term added, the Hamiltonian for the free atom is complete.

Crystal field splitting In octahedral and tetrahedral symmetry (both within the $\mathrm{O_h}$ point group) the one crystal field parameter is the crystal field splitting parameter, $10Dq$. CTM4XAS by default calculates for octahedral symmetry, so tetrahedral conditions need to use a negative value. While electrons in t_{2g} and e_g orbitals are mildly affected by changes in the crystal field strength, the biggest factor this controls is whether or not the system is low-spin (preferably paired valence electrons) or high-spin (preferably unpaired).

Charge transfer parameters In octahedral coordination there are five parameters relating to charge-transfer that can be modified in CTM4XAS.

Δ The energy difference in eV between a $3d^n$ state, with n electrons in the $3d$ orbitals, and a $3d^{n+1}\underline{\mathrm{L}}$ state, where an electron has transferred from the ligand to an unoccupied $3d$ orbital. A transfer of charge is likely to happen if the increase in energy is offset by a decrease in the energy of the entire system due to a core hole screening effect.

U_{dd} The intra-atomic coulomb interaction, or the resulting difference in energy after charge transfer due to electron-electron repulsion. Changing this parameter has no effect in simulated XPS spectra.

U_{pd} The electric potential due to the induced core hole. This has a direct effect on XPS spectra, but in XAS only the difference between U_{dd} and U_{pd} is relevant. By default this difference is set to 1 eV.

$T(e_g), T(t_{2g})$ Ligand covalent mixing parameters, also known as “hopping” parameters. Ostensibly these dictate the strength of orbital mixing between the $3d$ orbitals in the metal and the $3p$ orbitals in the ligand (sulfur). The larger these parameters are the higher the likelihood of charge transfer. These values are difference for the t_{2g} orbitals compared to the e_g depending on the crystal field symmetry. In octahedral coordination, $T(e_g)$ is always set to $2 \cdot T(t_{2g})$, whereas the opposite is true for tetrahedral coordination.

4 Results and discussion

4.1 XPS spectra

An XPS survey scan can be taken to identify the level of oxidation and carbon contamination of a surface. Goh et al. (2006) achieved a reasonably low level of oxidation (Figure 12(c)) with a natural pentlandite sample by by preparing the surface using abrasion. At the time this was considerably less oxidised than what had been seen in previous studies. Figure 12(a) show the survey scan of the vacuum fractured synthetic pentlandite sample surface used in this study, displaying significantly smaller oxygen and carbon peaks. XPS quantification of the survey spectrum showed atomic percentages of 44.5% S, 19.3% Fe, 19.0% Ni, 13.7% C, and 3.4% O. Considering the effects of surface-sensitive nature of XPS this shows good agreement to the stoichiometric ratios measured of iron, nickel, and sulfur. The presence of adventitious carbon would be due to the mild contamination of the source metal wire and sulfur powder prior to the synthetic pentlandite formation. The small but non-zero oxygen peak could be due to mild oxidation in vacuum.

A previous scan of vacuum fractured synthetic pentlandite taken by Harmer in 2014 (Figure 12 (b)) shows a slightly larger oxidation peak. While this data is not used in the study the Fe and Ni $2p$ XPS spectra will be compared for feature similarity and confirmation as extra information is available from its lower signal to noise ratio.

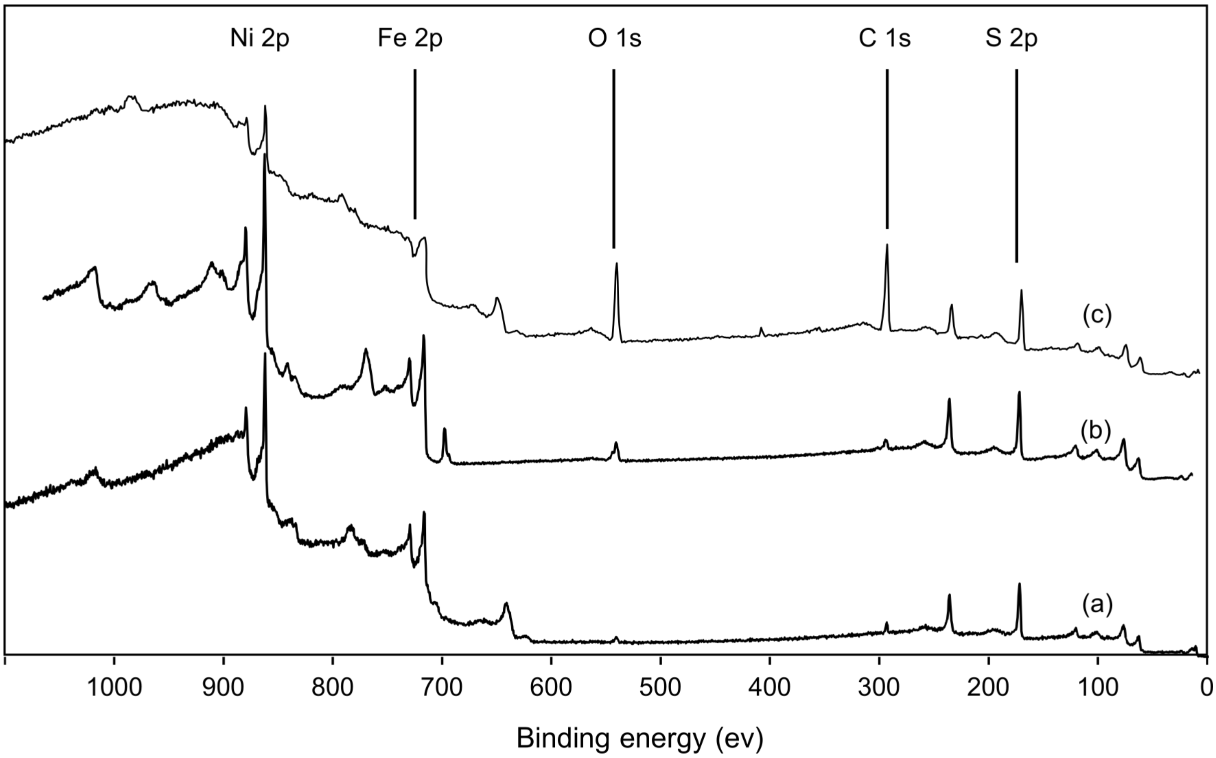

Figure 12: XPS survey scans of vacuum-fractured synthetic pentlandite (2014) (a), more oxidised sample collected by Harmer (2014) (b), and abraded natural pentlandite adapted from Goh (2006)[32] showing comparative levels of oxidation

High resolution Fe $2p$ XPS and Ni $2p$ spectra were taken with a photon energy of 1475 eV, shown in Figure 13. A single Shirley background was taken for Fe and two Shirley background were taken for Ni due to a single background unrealistically cutting through the data. The most significant feature present in the Fe XPS spectrum is the significant asymmetrical broadening in the higher energies of the $2p_{\frac{3}{2}}$ peak. The Ni spectrum shows a well-defined and symmetrical $2p_{\frac{3}{2}}$ peak but with two low-magnitude and broad features at approximately 856 eV and 860 eV, which are present in prior study[11].

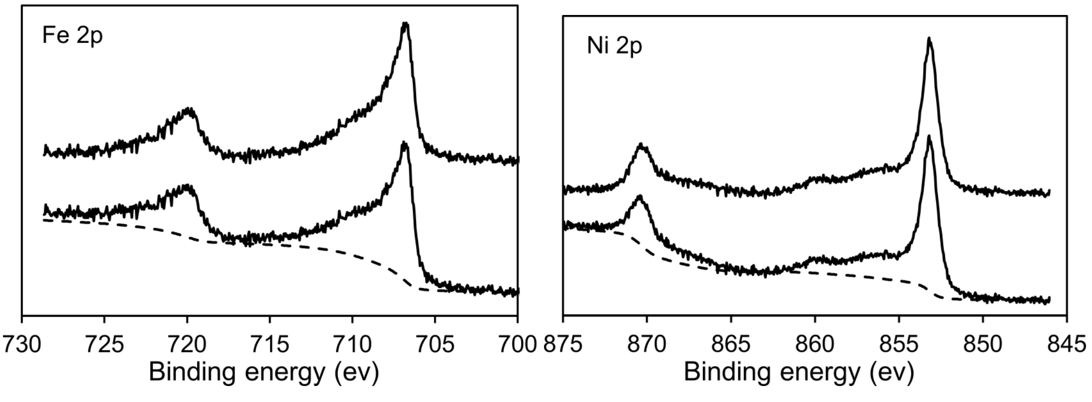

Figure 13: Raw pentlandite XPS signal (below, —), calculated Shirley background (- - -), and background subtracted spectrum (above, —) for iron and nickel

The Fe $2p$ and Ni $2p$ XPS spectra of the sample analysed in Figure 12 (b) are compared to those in 12 (a). The Fe spectrum of the more oxidised sample in Figure 14 shows a well-defined peak at 711 eV, which has been shown in previous studies to be an oxidation artefact[1;9;32]. Otherwise the two spectra are comparable. The Ni $2p$ spectrum of the more oxidised sample shows exactly the same features as in the cleaner sample, and the peaks are better defined due to lower noise. No oxidation features are evident, however it has been shown that iron strongly preferentially oxidises in synthetic pentlandite relative to nickel[1].

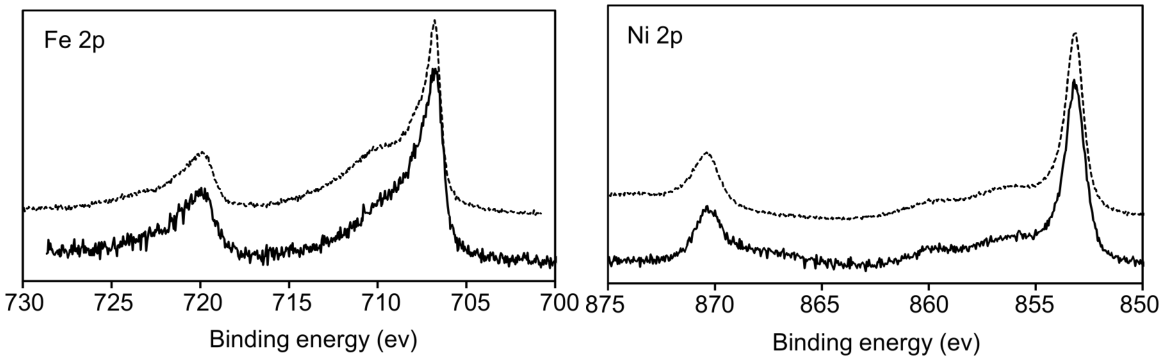

Figure 14: Comparison of processed XPS spectra for more ($\cdots$) and less (—) oxidised samples

4.2 NEXAFS spectra

Fe $L_{2,3}$ and Ni $L_{2,3}$ NEXAFS spectra were taken of the vacuum fractured synthetic pentlandite sample (Figure 15). After a linear background was subtracted from the pre- and post-edges, an arctan background was removed. The Fe $L_{2,3}$ spectrum shows two distinct qualities. Firstly, a convoluted but recognisable pre-edge peak at approximately 705.5 eV is present giving rise to a shoulder on the L_3 edge. This has been seen in previous study[14]. Secondly, a further post-edge broadening gives an asymmetric lineshape, which could be due to inadequate background subtraction but potentially due to further higher-energy transitions close to the L_3 edge. The most significant feature of the Ni $L_{2,3}$ spectrum is the broad secondary peak above the L_3 edge at 859 eV, which is duplicated above the L_2 edge at 867 eV.

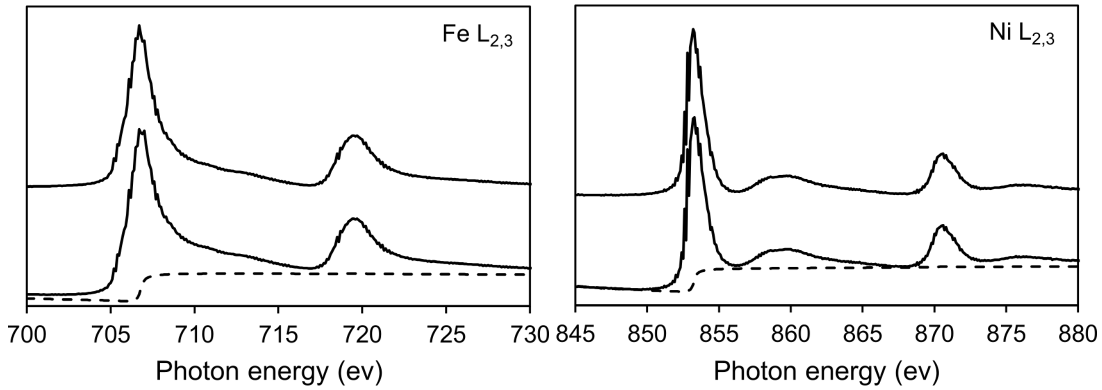

Figure 15: Raw pentlandite NEXAFS signal (below, —), calculated arctangent background (- - -), and background subtracted spectrum (above, —) for iron and nickel

4.3 Simulation

The two $4d$ electrons in both iron and nickel are using in the bonding process within pentlandite. As such, Fe^{2+} and Ni^{2+} spectra are calculated. The temperature is set to 298 K ($25°$C) as the samples were analysed at room temperature. For all simulations aside from the final, Gaussian broadening both Gaussian and Lorentzian broadening are set to 0.2. For the discussion of the results of this study, each electronic structure parameter is varied for four simulations to view their effects and the atomic, crystal, and charge transfer effects are built up to simulate the experimental system. These simulations are $2p$ Fe XAS, $L_{2,3}$ Fe XPS, $2p$ Ni XAS, and $L_{2,3}$Ni XPS. From here on in, XAS will be used to refer to the calculated spectra used to simulate NEXAFS data. Appropriateness of fit of the simulations to the data is qualitatively determined due to deficiencies in the accuracy of background subtraction.

4.3.1 Initial simulation

The initial simulations in Figure 16 show the resultant spectra when all electronic structure parameters are set to 0. The interpretation of the graph is that there is a single possible energy level in the $2p$ orbitals when no splitting effects are taken in to account. Whereas a typical XPS spectrum shows $2p_{\frac{3}{2}}$ and $2p_{\frac{1}{2}}$ peaks (or XAS shows L_3 and L_2 peaks), with no spin-orbit coupling there have the same energy. At this point, the XAS and XPS spectra are identical for a given atom, so the Fe XAS and Ni XPS spectra are presented.

F_{dd}	F_{pd}	G_{pd}	SO	$10Dq$	Δ	U_{dd}	U_{pd}	$T(e_g)$	$T(t_{2g})$
0	0	0	0	0	0	0	0	0	0

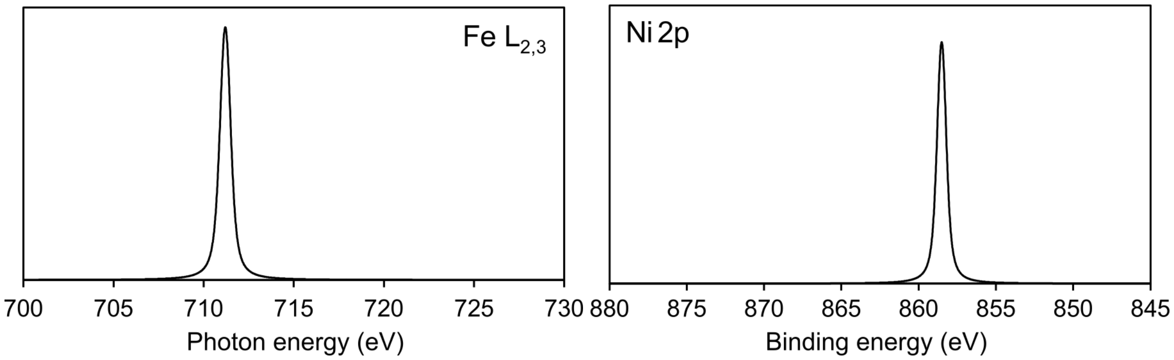

Figure 16: Initial simulations of iron XAS and nickel XPS with all parameters at 0

4.3.2 Spin-orbit coupling

To give an approximately representative shape to the spectra, the effect spin-orbit coupling is then added. In Figure 17 as the SO coupling strength is increased the singlet state becomes a doublet state and the peak areas show a constant $1:2$ ratio due to the degeneracy of the $2p_{\frac{1}{2}}$ and $2p_{\frac{3}{2}}$ states. A similar effect is seen in the XAS spectrum however the magnitude of the L$_2$ peak decreases as the SO coupling increases. In fact this transition is 0 when the temperature is set to 0, indicating the the the doublet $2p$ state in an XAS transition is only likely when heat is added to the system. Setting the SO coupling to the default value of 1 shows good splitting agreement with experimental data, and varying simply the valence SO coupling showed no appreciable difference in spectral features. While CTM4XAS gives the option to vary the core electron SO coupling these electrons are sufficiently well screened such that there should be no variance from the default value.

F_{dd}	F_{pd}	G_{pd}	SO	$10Dq$	Δ	U_{dd}	U_{pd}	$T(e_g)$	$T(t_{2g})$
0	0	0	x	0	0	0	0	0	0

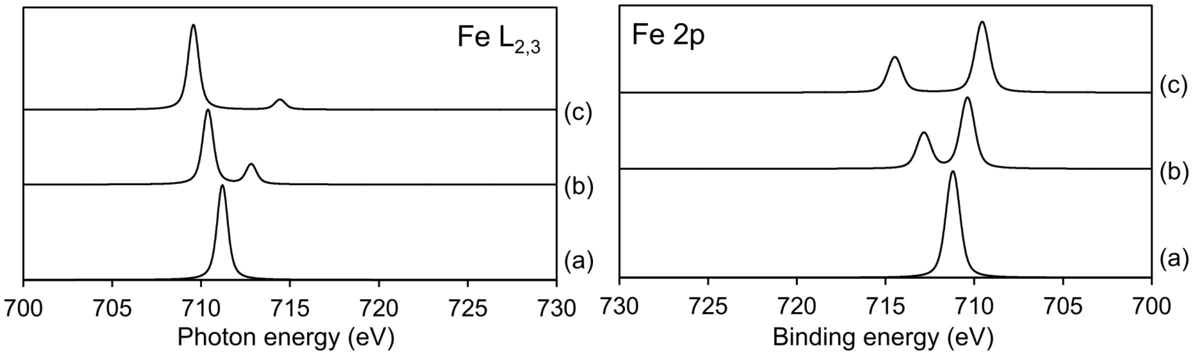

Figure 17: Spin-orbit coupling parameters set to 0 (a), 0.2 (b), and 0.4 (c) for iron XAS and XPS

4.3.3 Slater-Condon parameters

Before determining appropriate Slater-Condon parameter reduction values, the effects of each individual parameter are investigated in XAS without spin-orbit coupling. In Figure 18 (c) a doublet state is produced when accounting for only the d-electron Coulomb interaction F_{dd}. Turning on only the Coulomb interaction between core and valence electrons (F_{pd}) produces a large amount of multiplet splitting is seen due to the very large number of final states, seen in Figure 18 (b). Only including the multipole exchange interaction between core and valence electrons (G_{pd}) produces a different but similarly broad set of final states, seen in Figure 18 (a). Setting all Slater-Condon parameters to 1 (Figure 18 (d)) shows a narrower distribution reminiscent of a triplet state, made of many convoluted peaks. The decrease in available transitions would be due to fewer of the final states being accessible via selections rules.

F_{dd}	F_{pd}	G_{pd}	SO	$10Dq$	Δ	U_{dd}	U_{pd}	$T(e_g)$	$T(t_{2g})$
x	y	z	0	0	0	0	0	0	0

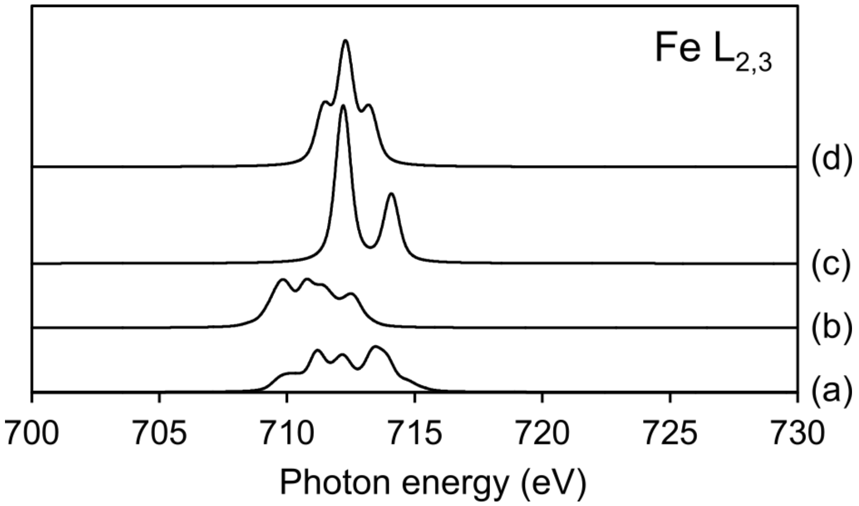

Figure 18: Fe XAS simulations where G_{pd} (a), F_{pd} (b), F_{dd} (c), and all three (d) are set to 1, all else 0

A simulated Fe XAS spectrum including both multiplet splitting and spin-orbit coupling is shown in figure Figure 19 (a). The crystal field splitting plays a significant role in the spectral shape, so it is introduced before determining an appropriate Slater-Condon parameter reduction. In octahedral coordination the default value for crystal field splitting parameter $10Dq$ is 1 eV. Because of the $8:1$ ratio of tetrahedral to octahedral metal coordination in pentlandite it can be assumed that the experimental XPS and NEXAFS spectra are representative of purely tetrahedral sites (de Groot, personal communication). Theoretically, the strength of crystal field splitting is $\frac{4}{9} \approx 0.44$ of the magnitude of octahedral, and in the reverse direction. Thus, the $10Dq$ is initially set to -0.44, shown in 19 (b).

F_{dd}	F_{pd}	G_{pd}	SO	$10Dq$	Δ	U_{dd}	U_{pd}	$T(e_g)$	$T(t_{2g})$
1	1	1	1	x	0	0	0	0	0

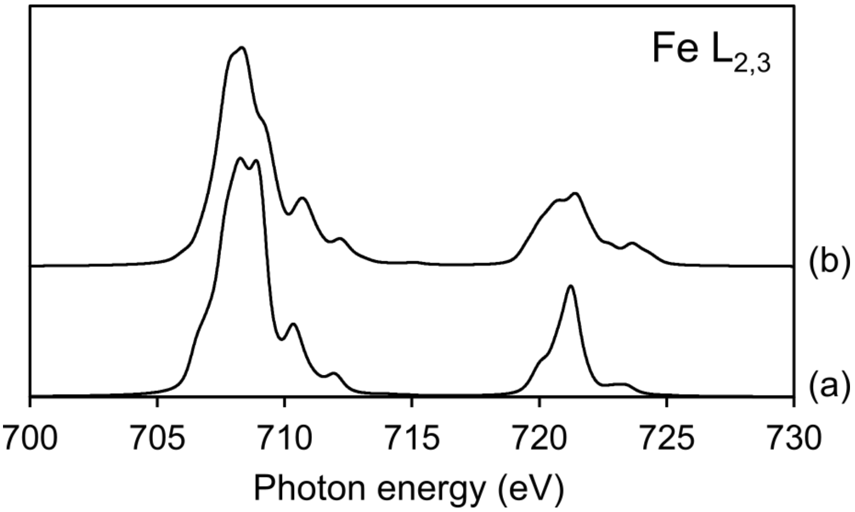

Figure 19: $10Dq$ set to 0 (a) and -0.44 (b) for iron XAS

The Slater-Condon parameter reduction for Fe and Ni XAS is varied from 1 to 0.2, shown in Figure 20. Broadly this shows a decrease in the magnitude of multiplet splitting. When set to 1 (a), the spectra show far more multiplet structure than what is seen in the NEXAFS data, however below 0.6 (c) the characteristic secondary peak in the Ni spectrum becomes unrealistically small.

F_{dd}	F_{pd}	G_{pd}	SO	$10Dq$	Δ	U_{dd}	U_{pd}	$T(e_g)$	$T(t_{2g})$
x	x	x	1	-0.44	0	0	0	0	0

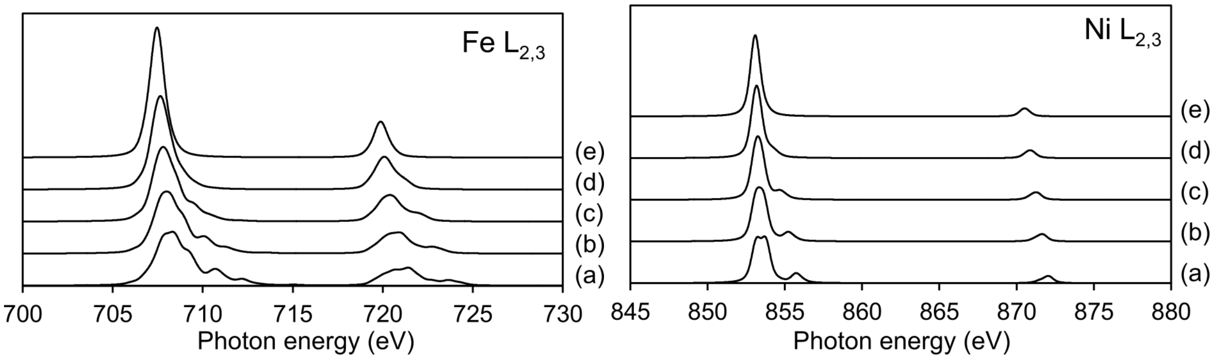

Figure 20: Slater-Condon parameters set to 1 (a), 0.8 (b), 0.6 (c), 0.4 (d), and 0.2 (e) for iron and nickel XAS

The same variance of Slater parameters is shown for Fe and Ni XPS in Figure21. While none of the spectra successfully recreate the experimentally data, it can be seen that a value of 0.2 removes too much of the multiplet structure, and values of 0.8 and 1.0 shows significantly more splitting, especially in the Fe spectra. A value of 0.6 is thus taken for its apparent appropriateness in both XPS and XAS.

F_{dd}	F_{pd}	G_{pd}	SO	$10Dq$	Δ	U_{dd}	U_{pd}	$T(e_g)$	$T(t_{2g})$
x	x	x	1	-0.44	0	0	0	0	0

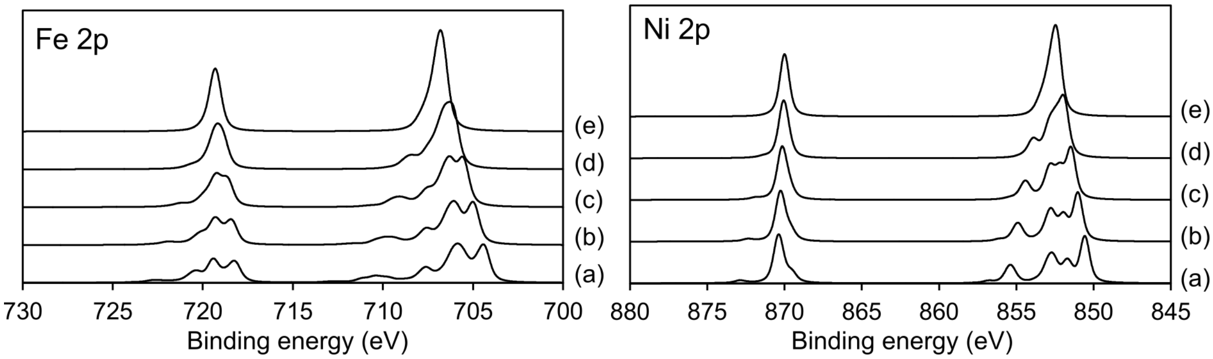

Figure 21: Parameters as in Figure 20, for iron and nickel XPS

4.3.4 Crystal field splitting

Octahedrally coordinated Fe^{2+} in pentlandite exists in the low-spin state, where the crystal field splitting energy is larger than the electron pairing energy. The magnitude of the crystal field splitting in tetrahedral coordination then shouldn't imply a $10Dq$ that results in high-spin octahedral iron. Figure 22 shows the result of increasing $10Dq$ for octahedral Fe XPS spectra. Negligable change in the spectrum is seen from 0.3 (a) to 0.4 eV (b), but at 0.5 eV (d) a sudden and large shift in spectral features takes place, indicating a shift to the high-spin state. Thus a lower bound for the tetrahedral $10Dq$ is $\frac{4}{9} \cdot 0.4 \approx 0.17$.

F_{dd}	F_{pd}	G_{pd}	SO	$10Dq$	Δ	U_{dd}	U_{pd}	$T(e_g)$	$T(t_{2g})$
0.6	0.6	0.6	1	x	0	0	0	0	0

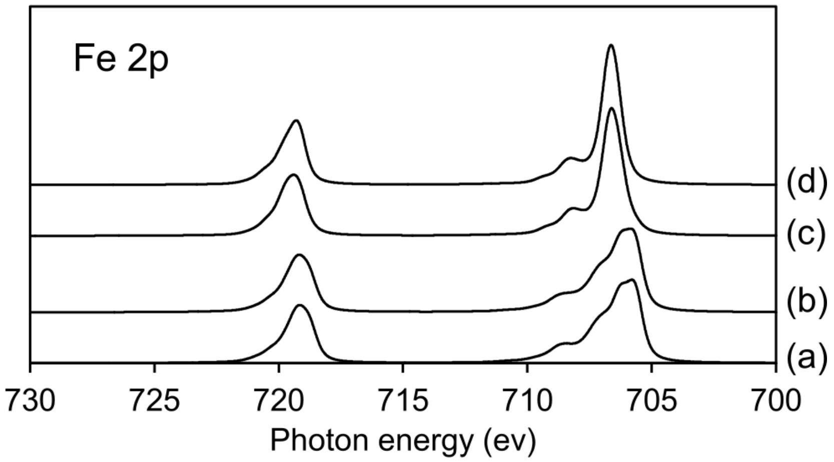

Figure 22: $10Dq$ set to 0.2 (a), 0.3 (b), 0.4 (c), and 0.5 eV (d) for iron XPS

Figure 23 shows the variance in XAS spectra when for values of $10Dq$ from -0.2 to -0.6. No significant changes in spectral features are seen.

F_{dd}	F_{pd}	G_{pd}	SO	$10Dq$	Δ	U_{dd}	U_{pd}	$T(e_g)$	$T(t_{2g})$
0.6	0.6	0.6	1	x	0	0	0	0	0

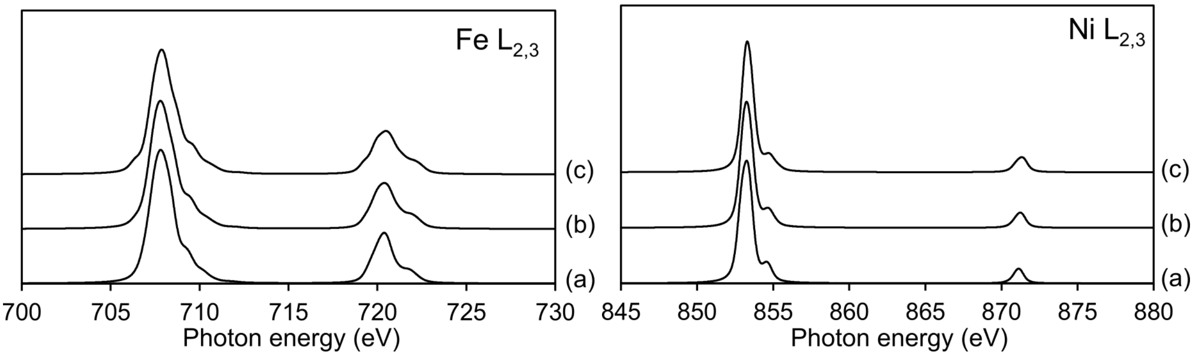

Figure 23: $10Dq$ set to -0.2 (a), -0.4 (b), and -0.6 (c) for iron and nickel XAS

Figure 24 shows the same range of $10Dq$ values in XPS spectra. While there are small changes in the relative heights of some peaks, no changes are significant enough to argue the preference of any particular $10Dq$ value. A moderate value of 0.4 is then used.

F_{dd}	F_{pd}	G_{pd}	SO	$10Dq$	Δ	U_{dd}	U_{pd}	$T(e_g)$	$T(t_{2g})$
0.6	0.6	0.6	1	x	0	0	0	0	0

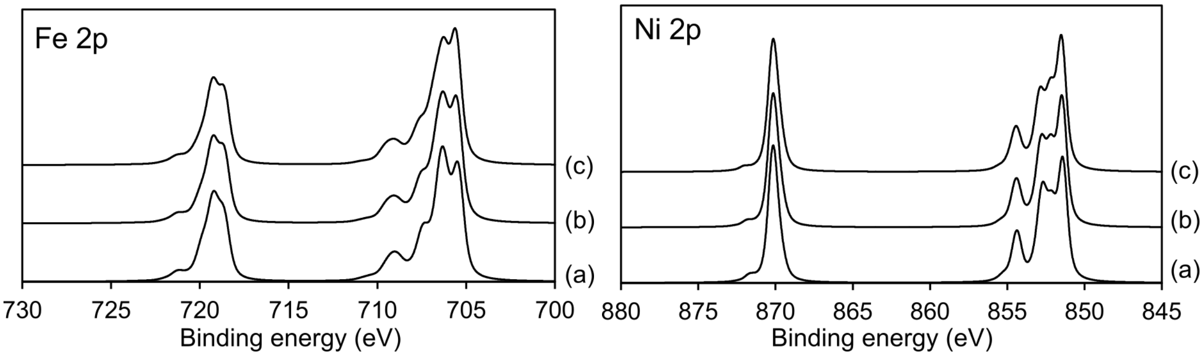

Figure 24: Parameters as in Figure 23 for iron and nickel XPS

4.3.5 Hopping parameters

Figure 25 shows the effect of varying the hopping parameters $T(e_g)$ and $T(t_{2g})$ for XAS. The values of these are kept at a constant $1:2$ ratio due to the geometry of the t_{2g} and e_g orbitals[33]. This ratio would be inverted if in octahedral coordination. Increasing these parameters from creates an a pre-edge charge transfer peak in the Fe XAS spectrum. This is fortunate as such a peak is seen in the experimental data. Furthermore, the secondary peak in Ni XAS is shifted to a higher energy, also more accurately representing the data. The magnitude of the Fe pre-edge peak becomes unrealistically large with values of 1.5 and 3 (c), and similarly the secondary peak move too too high an energy.

F_{dd}	F_{pd}	G_{pd}	SO	$10Dq$	Δ	U_{dd}	U_{pd}	$T(e_g)$	$T(t_{2g})$
0.6	0.6	0.6	1	-0.4	0	0	0	x	$2x$

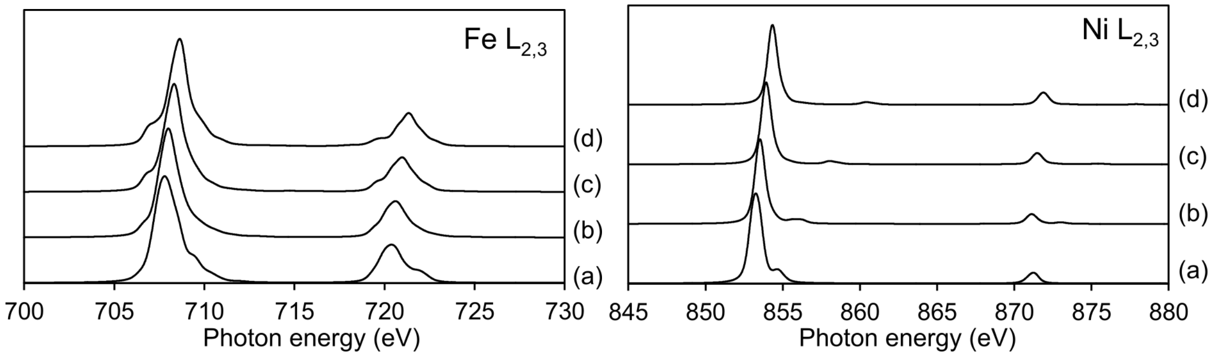

Figure 25: $T(e_g)$ set to 0.5 (a), 1 (b), 1.5 (c), and 2 (d) for iron and nickel XAS, with $T(t_{2g})$ set to $2 \cdot T(e_g)$

Figure 26 shows the same variance of the hopping parameters in XPS. Increasing the likelihood of charge transfer appears to decrease the multiplet splitting structure in XPS, which is well-understood in literature[33]. Values of 0.5 and 1 (a) display too much multiplet splitting in Fe XPS, while values of 2 and 4 show too little broadening. All values aside from 0.5 and 1 (a) have the potential to be appropriate for Ni XPS. Values of 1 and 2 are settled upon for $T(e_g)$ and $T(t_{2g})$ respectively due to their appropriateness in both XPS and XAS spectra.

F_{dd}	F_{pd}	G_{pd}	SO	$10Dq$	Δ	U_{dd}	U_{pd}	$T(e_g)$	$T(t_{2g})$
0.6	0.6	0.6	1	-0.4	0	0	0	x	$2x$

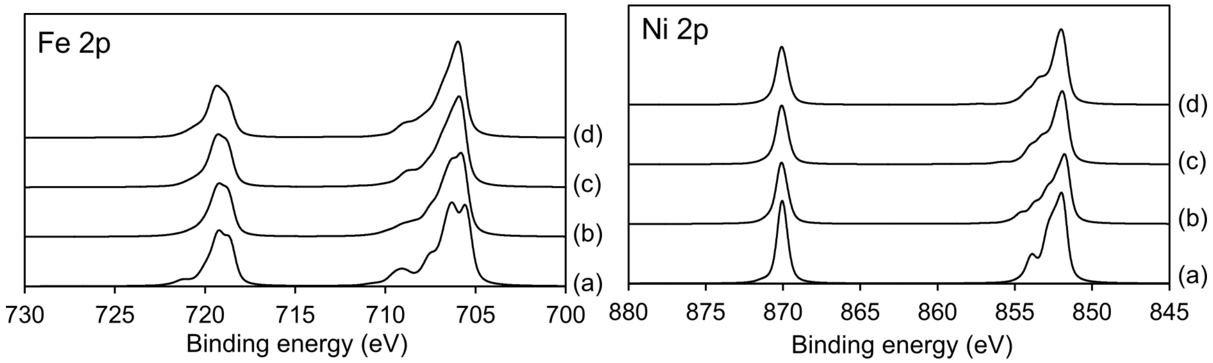

Figure 26: Parameters as in Figure 23 for iron and nickel XPS

4.3.6 Intra-atomic Coulomb interaction and core hole potential

In XAS spectra the difference between U_{dd} (intra-atomic Coulomb interaction) and U_{pd} (core hole potential) values has an effect on spectral features but the individual values of these parameters do not. Thus, U_{dd} is kept at 0 and U_{pd} is varied. A difference of approximately 1 eV is to be expected[27]. Indeed, Figure 27 shows that a difference greater than 1 increases the magnitude of a peak at 714 eV in the Fe XAS spectrum, which is not seen in the data. A lower value however decreases the 858 eV peak in the Ni XAS spectrum, which is evident in the data. Thus the default difference of 1 is kept.

F_{dd}	F_{pd}	G_{pd}	SO	$10Dq$	Δ	U_{dd}	U_{pd}	$T(e_g)$	$T(t_{2g})$
0.6	0.6	0.6	1	-0.4	0	0	x	1	2

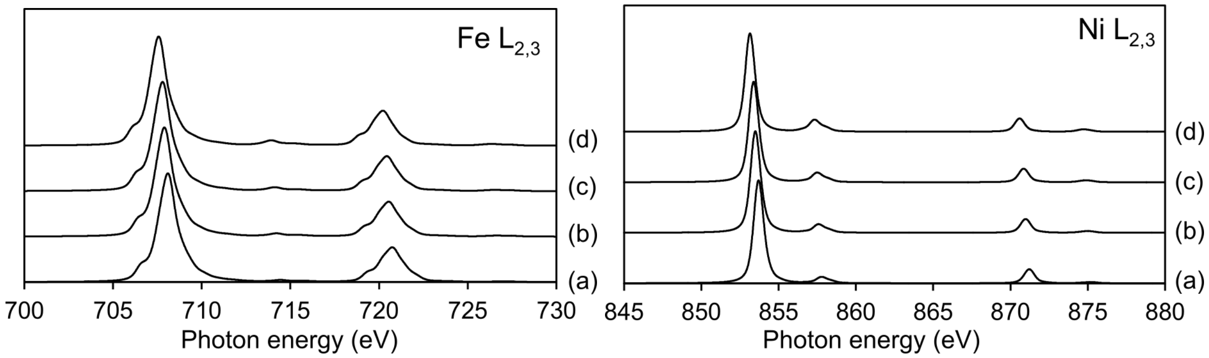

Figure 27: U_{pd} set to 0.6 (a), 0.9 (b), 1.1 (c), and 1.4 (d) for iron and nickel XAS

Conversely, in XPS only the value of U_{pd} matters. Varying U_{dd} makes no change. Figure 28 shows the effect of increasing U_{pd} from 0 to 6 eV. In the Fe spectrum this creates secondary peaks at at 712 eV and 725 eV, but they don't have significant magnitudes until $U_{pd} = 6$ (d). The effect in the Ni spectrum is important; increasing U_{pd} produces groups of peak at energies slightly higher than L$_3$ edge, energies at which features are seen in the data. At or below $U_{pd} = 2$ these features are too small. A U_{pd} of 4 is then settled on, and therefore so is a U_{dd} is 3.

F_{dd}	F_{pd}	G_{pd}	SO	$10Dq$	Δ	U_{dd}	U_{pd}	$T(e_g)$	$T(t_{2g})$
0.6	0.6	0.6	1	-0.4	0	0	x	1	2

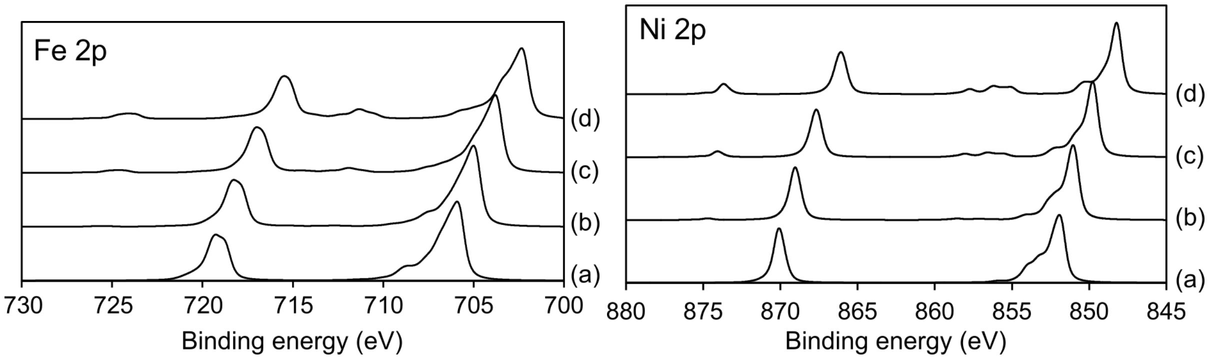

Figure 28: U_{pd} set to 0 (a), 2 (b), 4 (c), and 6 (d) for iron and nickel XPS

4.3.7 Charge transfer energy

Figure 29 shows that increasing the charge transfer energy Δ does very little to XAS spectra except to decrease the magnitude of the secondary peaks in nickel, which is not preferred for an accurate simulation.

F_{dd}	F_{pd}	G_{pd}	SO	$10Dq$	Δ	U_{dd}	U_{pd}	$T(e_g)$	$T(t_{2g})$
0.6	0.6	0.6	1	-0.4	x	3	4	1	2

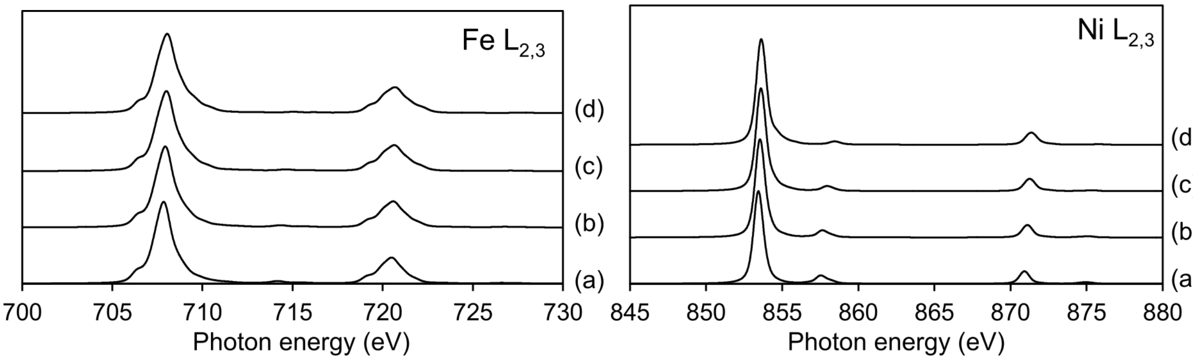

Figure 29: Δ set to 0 (a), 1 (b), 2 (c), and 3 (d) for iron and nickel XAS

In XPS, Figure 30 shows that increasing Δ makes the features around 851 eV in Ni stronger, which is not seen in the data. It also adds a small feature at 707 eV in the Fe spectrum, which is again not seen in spectra.

F_{dd}	F_{pd}	G_{pd}	SO	$10Dq$	Δ	U_{dd}	U_{pd}	$T(e_g)$	$T(t_{2g})$
0.6	0.6	0.6	1	-0.4	x	3	4	1	2

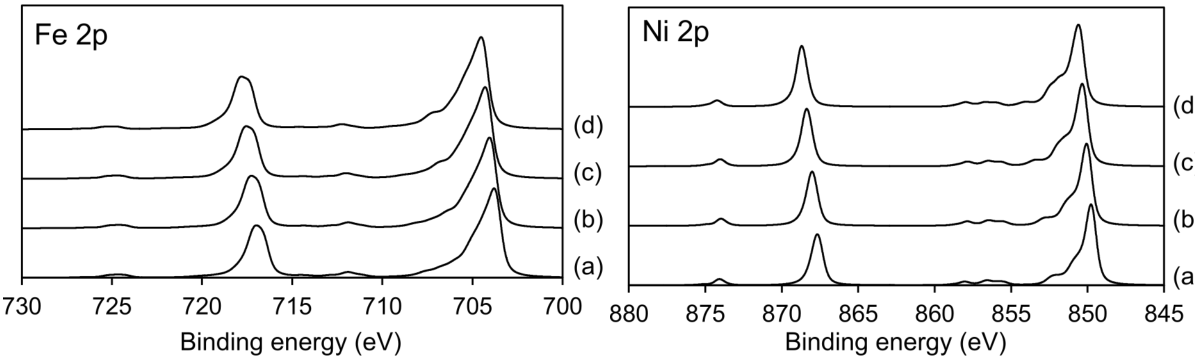

Figure 30: Parameters as in Figure 29 for iron and nickel XPS

Given the very little difference in spectra between $\Delta = 0$ and $\Delta = 1$, an upper limit of 1 eV is chosen.

4.4 Final parameters

For comparing the final simulations to the data, the peaks were shifted so that the main peaks lined up with those in the data. The simulated energies are accurate relative to each other but the overall energies are known to vary slightly from real values. Furthermore, the F_{pd} and G_{pd} values are reduced to 0.5, while keeping F_{dd} at 0.6. This has multiple effects which improve the accuracy of the simulations. Lastly the “sticks”, or the individually calculated transition energies and their magnitudes, are shown underneath the data.

Figure 31 shows a good reproduction of the Fe NEXAFS lineshape. Most importantly the pre-edge peak is successfully reproduced at an energy and magnitude close that that seen in data. A slight reduction of the F_{pd} and G_{pd} values shifts this peak to a slightly higher energy. Because this features appears due to an increase in the hopping parameters it can be concluded that it's a charge transfer satellite. At the energy of approximately 705.5 eV an electron transfer from the sulfur $3p$ to an unoccupied iron $3d$ orbital can noticeably reduce the energy of the system after an Fe $2p$ to $3d$ excitation.

F_{dd}	F_{pd}	G_{pd}	SO	$10Dq$	Δ	U_{dd}	U_{pd}	$T(e_g)$	$T(t_{2g})$
0.6	0.5	0.5	1	-0.4	1	3	4	1	2

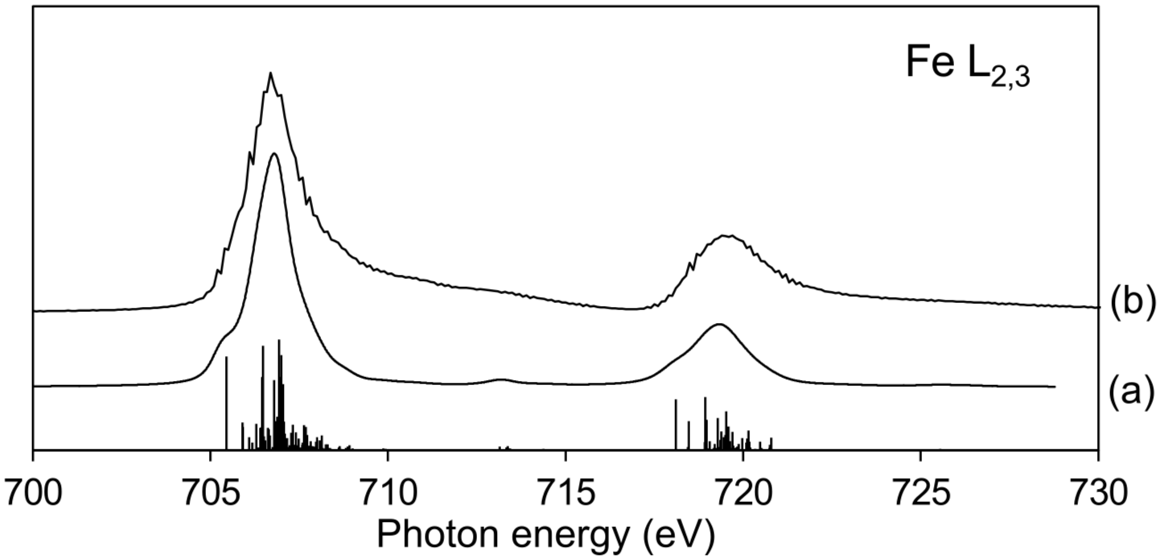

Figure 31: Comparison of final iron XAS simulation (a) to iron NEXAFS data (b) with sticks underneath

Figure 32 shows a good reproduction of the general Ni NEXAFS lineshape. While the energies and magnitudes of the secondary features are slightly lower than in the data, the existence of the features is indicative of a reasonably accurate set of parameters. Furthermore no other extraneous spectral features are observed in the data or the simulation. The secondary features were seen to be the result of multiplet splitting.

F_{dd}	F_{pd}	G_{pd}	SO	$10Dq$	Δ	U_{dd}	U_{pd}	$T(e_g)$	$T(t_{2g})$
0.6	0.5	0.5	1	-0.4	1	3	4	1	2

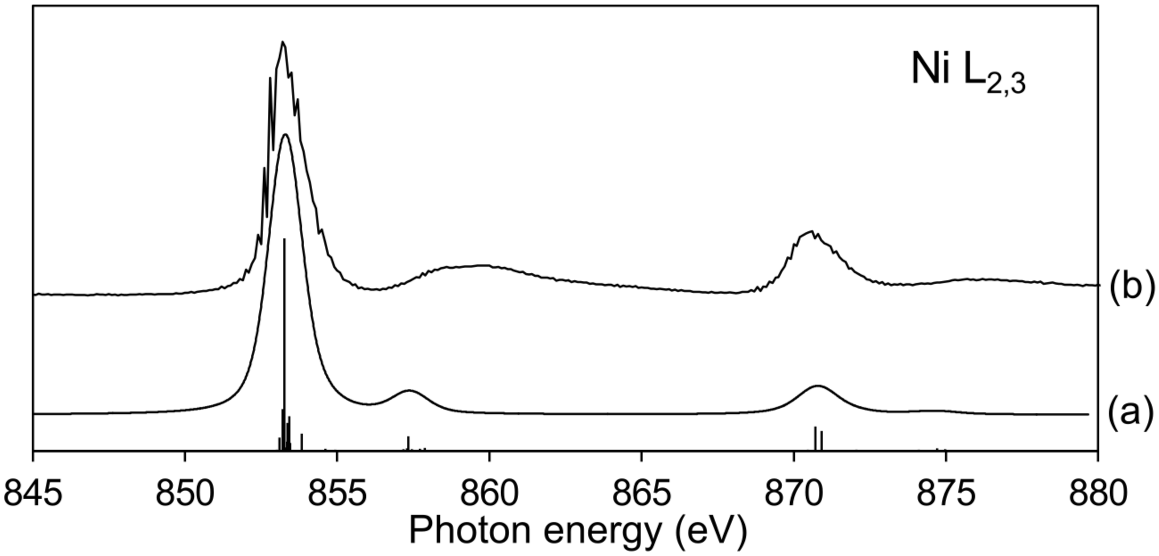

Figure 32: Comparison of final nickel XAS simulation (a) to nickel NEXAFS data (b) with sticks underneath

Figure 33 shows a good reproduction of the Fe XPS lineshape. Of note is the asymmetrical broadening of the $2p_{\frac{3}{2}}$ peak which is successfully reproduced and present due to multiplet splitting. The data displays wider broadening which may be due to an inadequate background subtraction or from very mild oxidation effects. The reduction of F_{pd} and G_{pd} reduced this simulated broadening slightly. The simulated feature at 715 eV is minimal, and the magnitude of the noise in the data could be obscuring such a feature.

F_{dd}	F_{pd}	G_{pd}	SO	$10Dq$	Δ	U_{dd}	U_{pd}	$T(e_g)$	$T(t_{2g})$
0.6	0.5	0.5	1	-0.4	1	3	4	1	2

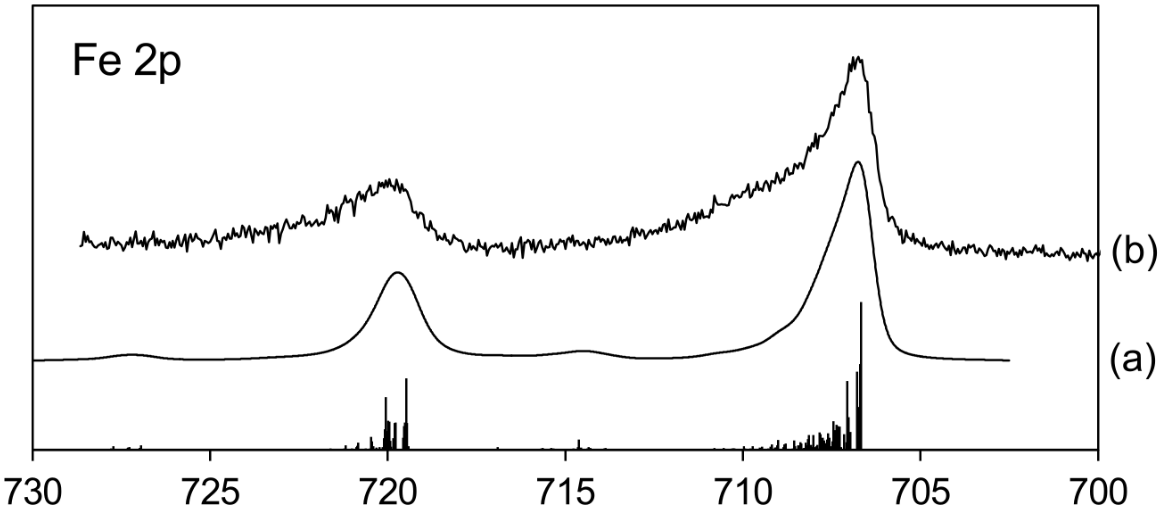

Figure 33: Comparison of final iron XPS simulation (a) to iron XPS data (b) with sticks underneath

Figure 34 shows a good reproduction of the Ni XPS lineshape. The reduction of F_{pd} and G_{pd} reduced the magnitude of the feature at 854 eV, which improves the appropriateness of the simulation. Of particular note are the features in the data between 855 and 860 eV. While not perfectly reproduced, these appear to be charge-transfer satellites strongly influenced by the magnitude of the core hole potential U_{pd}.

F_{dd}	F_{pd}	G_{pd}	SO	$10Dq$	Δ	U_{dd}	U_{pd}	$T(e_g)$	$T(t_{2g})$
0.6	0.5	0.5	1	-0.4	1	3	4	1	2

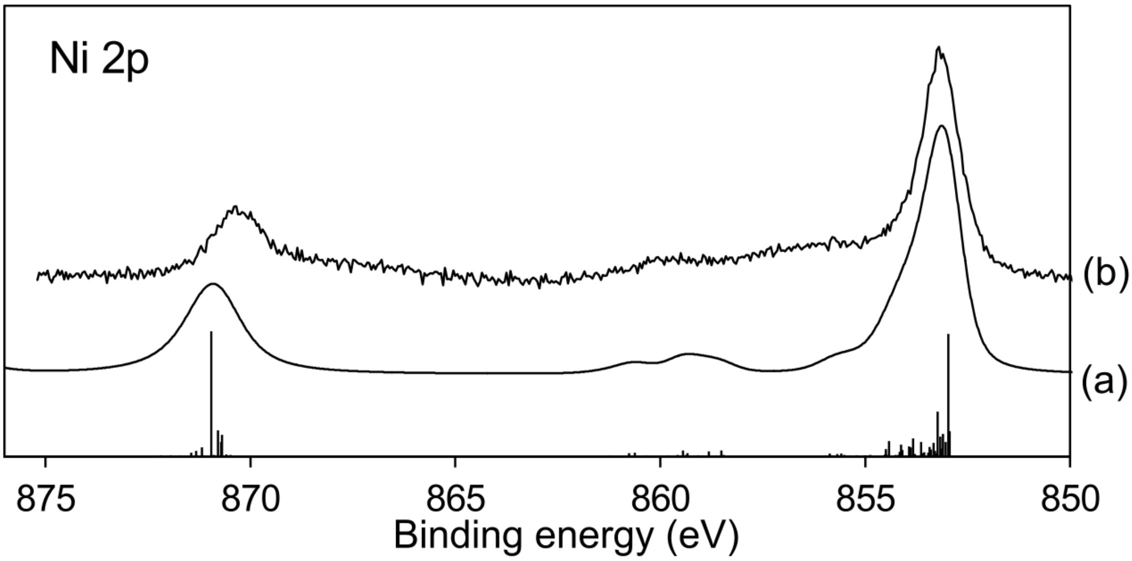

Figure 34: Comparison of final nickel XPS simulation (a) to nickel XPS data (b) with sticks underneath

5 Conclusion

A sample of synthetic pentlandite was created and high-resolution synchrotron XPS $2p$ and NEXAFS L$_{2,3}$ spectra were collected for iron and nickel. The lineshapes of these spectra were reproduced with good approximation with CTM4XAS using the following electronic structure parameters:

F_{dd}	F_{pd}	G_{pd}	SO	$10Dq$	Δ	U_{dd}	U_{pd}	$T(e_g)$	$T(t_{2g})$
0.6	0.5	0.5	1	-0.4	1	3	4	1	2

The pentlandite Fe NEXAFS pre-edge feature was succesfully reproduced and identified as being a charge-transfer satellite due to an electron hopping from the sulfur $3p$ to iron $3d$ orbitals. The charge transfer energy Δ for pentlandite was shown to have an upper bound of 1 eV. Secondary features present in pentlandite Ni NEXAFS were concluded to be due to multiplet splitting effects. Post-edge features present in pentlandite Ni XPS , which are observable in previous studies, were shown to be due to charge transfer with their presence highly dependant on the magnitude of the core hole potential.

6 Future work

Future electronic structure study of synthetic pentlandite can be undertaken using the Resonant Inelastic X-ray Scattering spectrsocopy technique where the relationship between the incident photon energy and intensities of final states can be directly measured. Figure 35 shows a simulated RIXS spectrum using the final electronic structure parameters as determined in this study.

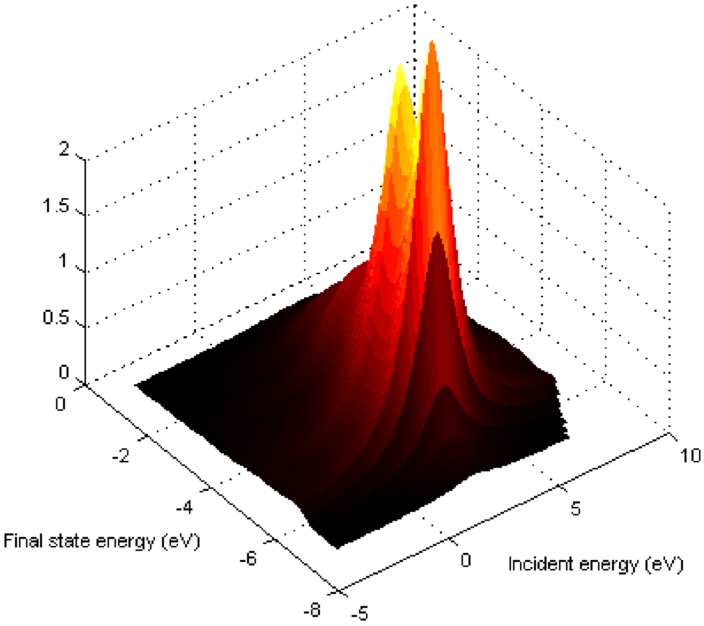

Figure 35: Simulated $1s2p$ RIXS for iron

With a better understanding of the eletcornic structure of pentlandite the opportunity arises for novel applications of the mineral to be investigated, such as in the field of microelectronics.

References

[1] S. Richardson and D. J. Vaughan. Surface alteration of pentlandite and spectroscopic evidence for secondary violarite formation. *Mineralogical Magazine*, 53:213–22, 1989.

[2] Statistia. Major countries in worldwide nickel mine production from 2010 to 2015, 2016.

[3] A.D. Pearson and M.J. Buerger. Confirmation of the crystal structure of pentlandite. *American Mineralogist*, 41, 1956.

[4] Getrude Marape. *Fundamental electrochemical behaviour of pentlandite*. 2010.

[5] M Lindqvist, D Lundqvist, and A Westgren. The crystal structure of co9s8 and of pentlandite (ni, fe) 9s8. *Kemisk Tidskrift*, 48:156–160, 1936.

[6] V Rajamani and CT Prewitt. Crystal chemistry of natural pentlandites. *The Canadian Mineralogist*, 12(3):178–187, 1973.

[7] Osvald Knop, Chung-Hsi Huang, and F.W.D. Woodhams. Chalcogenides of the transition elements. vii. a mossbauer study of pentlandite. *The American Mineralogist*, 55, 1970.

[8] Katsuhiro Tsukimura. Fe/ni distribution in pentlandite at high temperature and the estimated pressure-temperature dependence of the distribution. *Mineralogical Journal*, 14(8):323–337, 1989.

[9] A. N. Buckley and R. Woods. Surface composition of pentlandite under flotation-related conditions. *Surface and Interface Analysis*, 17(9):675–680, aug 1991.

[10] AN Buckley, IC Hamilton, and R Woods. Developments in mineral processing flotation of sulfide minerals, edited by kse forssberg, 1985.

[11] D.L. Legrand, G.M. Bancroft, and H.W. Nesbitt. Surface characterization of pentlandite, (fe,ni)9s8, by x-ray photoelectron spectroscopy. *International Journal of Mineral Processing*, 51(14):217 – 228, 1997. Application of Surface Science to Advancing Flotation Technology.

[12] R. P. Gupta and S. K. Sen. Calculation of multiplet structure of core p-vacancy levels. ii. *Phys. Rev. B*, 12:15–19, Jul 1975.

[13] Siew Wei Goh, Alan N. Buckley, Robert N. Lamb, Liang-Jen Fan, Ling-Yun Jang, and Yaw-wen Yang. Pentlandite sulfur core electron binding energies. *Physics and Chemistry of Minerals*, 33(7):445–456, 2006.

[14] Robert George Acres, Sarah Louise Harmer, and David Allan Beattie. Synchrotron PEEM and ToF-SIMS study of oxidized heterogeneous pentlandite, pyrrhotite and chalcopyrite. *Journal of Synchrotron Radiation*, 17(5):606–615, Sep 2010.

[15] Piter S Miedema, Matti M van Schooneveld, Rene Bogerd, Tulio CR Rocha, Michael Havecker, Axel Knop-Gericke, and Frank MF de Groot. Oxygen binding to cobalt and iron phthalocyanines as determined from in situ x-ray absorption spectroscopy. *The Journal of Physical Chemistry C*, 115(51):25422–25428, 2011.

[16] A Nyrow, C Sternemann, M Wilke, RA Gordon, K Mende, H Yavas, L Simonelli, N Hiraoka, Ch J Sahle, S Huotari, et al. Iron speciation in minerals and glasses probed by m2/3-edge x-ray raman scattering spectroscopy. *Contributions to mineralogy and petrology*, 167(5):1–13, 2014.

[17] Gosuke Oyama, Hisao Kiuchi, Sai Cheong Chung, Yoshihisa Harada, and Atsuo Yamada. Combined experimental and computational analyses on the electronic structure of alluaudite-type sodium iron sulfate. *The Journal of Physical Chemistry C*, 2016.

[18] Mustafa Al Samarai, Mario Ulises Delgado-Jaime, Hirofumi Ishii, Nozomu Hiraoka, Ku-Ding Tsuei, Jean-Pascal Rueff, Benedikt Lassalle-Kaiser, Bert M Weckhuysen, and Frank MF de Groot. 1s3p resonant inelastic x-ray scattering of cobalt oxides and sulfides. *The Journal of Physical Chemistry C*, 2016.

[19] IRAMIS. X-ray photoelectrons spectroscopy (xps), 2016.

[20] Paul S. Bagus, Eugene S. Ilton, and Connie J. Nelin. The interpretation of xps spectra: Insights into materials properties. *Surface Science Reports*, 68(2):273–304, jun 2013.

[21] C. Hébert. Practical aspects of running the wien2k code for electron spectroscopy. *Micron*, 38(1):12 – 28, 2007.

[22] John C. Fuggle and John E. Inglesfield. Unoccupied electronic states. 1992.

[23] Georg Hahner. Near edge x-ray absorption fine structure spectroscopy as a tool to probe electronic and structural properties of thin organic films and liquids. *Chem. Soc. Rev.*, 35:1244–1255, 2006.

[24] Kieron Burke, Lucas Wagner, Miles Stoudenmirem, and Steve White. Failures of density functional theory for strongly correlated systems using density-matrix renormalization group. Departmentsof Physics and of Chemistry UC Irvine, 2013.

[25] Christine M Isborn, Brendan D Mar, Basile FE Curchod, Ivano Tavernelli, and Todd J Martínez. The charge transfer problem in density functional theory calculations of aqueously solvated molecules. *The Journal of Physical Chemistry B*, 117(40):12189–12201, 2013.

[26] Dionys Baeriswyl, David K Campbell, Jose MP Carmelo, Francisco Guinea, and Enrique Louis. *The Hubbard model: its physics and mathematical physics*, volume 343. Springer Science & Business Media, 2013.

[27] Frank de Groot. Multiplet effects in x-ray spectroscopy. *Coordination Chemistry Reviews*, 249(1):31–63, 2005.

[28] Doug Hatfield. Hydrogen orbitals 3d real. *Wikimedia Commons*, 2008.

[29] M Repoux. Comparison of background removal methods for xps. *Surface and Interface Analysis*, 18(7):567–570, 1992.

[30] Ralf Vanselow and Russell F Howe. *Chemistry and physics of solid surfaces VII*, volume 10. Springer Science & Business Media, 2012.

[31] Eli Stavitski and Frank M.F. de Groot. The CTM4xas program for EELS and XAS spectral shape analysis of transition metal l edges. *Micron*, 41(7):687–694, oct 2010.

[32] Siew Wei Goh. *Application of surface science to sulfide mineral processing*. PhD thesis, Chemistry, Faculty of Science, UNSW, 2006.

[33] Frank de Groot and Akio Kotani. *Core level spectroscopy of solids*. CRC press, 2008.